*minerals*

MDPI

*Article*

# Mesozoic Northward Subduction Along the SE Asian Continental Margin Inferred from Magmatic Records in the South China Sea

**Guanqiang Cai [1], Zhifeng Wan [2,3,*], Yongjian Yao [1,*], Lifeng Zhong [3], Hao Zheng [2,3], Argyrios Kapsiotis [2,3] and Cheng Zhang [2]**

1 Guangzhou Marine Geological survey, Guangzhou 510760, China; caiguanqiang@sina.com
2 School of Marine Sciences, Sun Yat-Sen University, Guangzhou 510006, China; zhengh66@mail.sysu.edu.cn (H.Z.); kapsiotis@mail.sysu.edu.cn (A.K.); zhangch83@mail2.sysu.edu.cn (C.Z.)
3 Southern Marine Science and Engineering Guangdong Laboratory (Zhuhai), Zhuhai 519082, China; zhonglf9@mail.sysu.edu.cn
* Correspondence: wanzhif@mail.sysu.edu.cn (Z.W.); yjyaomail@163.com (Y.Y.)

Received: 29 August 2019; Accepted: 27 September 2019; Published: 30 September 2019




**Abstract:** During the Mesozoic, Southeast (SE) Asia (including South China and the South China Sea (SCS)) was located in a transitional area between the Tethyan and Pacific geotectonic regimes. However, it is unclear whether geodynamic processes in the SE Asian continental margin were controlled by Tethyan or paleo-Pacific Ocean subduction. Herein, we report ~124 Ma adakitic granodiorites and Nb-enriched basalts from the Xiaozhenzhu Seamount of the SCS. Granodiorites have relatively high Sr/Y (34.7–37.0) and $(La/Yb)_N$ (13.8–15.7) ratios, as well as low Y (9.67–9.90 μg/g) and Yb (0.93–0.94 μg/g) concentrations, typical of adakites. Their Sr/Y and $(La/Yb)_N$ values coupled with their relatively low initial $^{87}Sr/^{86}Sr$ ratios (0.70541–0.70551), relatively high $K_2O$ contents (3.31–3.38 wt%), high Th/La ratios (0.33–0.40), negative $\varepsilon_{Nd}(t)$ values (−3.62 to −3.52), and their variable zircon $\varepsilon_{Hf}(t)$ values (−3.8 to +5.2) indicate that these rocks were formed by melting of subducted oceanic crust and sediments. The Nb-enriched basalts show enrichment in high field strength elements (HFSE) and have $\varepsilon_{Nd}(t)$ values of +2.90 to +2.93, as well as relatively low initial $^{87}Sr/^{86}Sr$ ratios of 0.70341–0.70343, demonstrating that they were derived from a depleted-mantle (DM) source metasomatized by silicate magmas originating from melting of a subducted oceanic lithospheric slab. By combining our findings with data from other Late Mesozoic arc-related magmatic rocks and adakites from the broader study area, we propose a geotectonic model involving subduction of young oceanic lithosphere during the Late Jurassic and northward subduction of the proto-South China Sea (PSCS) along the SE Asian continental margin during the Early Cretaceous. This conceptual model better explains the two-period Mesozoic magmatism, commonly reported for the SE Asian continental margin.

**Keywords:** granodiorite; Nb-enriched basalt; SE Asia; continental margin; South China Sea

## 1. Introduction

During the Cenozoic Era, the Southeast (SE) Asian region underwent substantial geological changes related mainly to the Indo–Asia collision. The region has thus attracted considerable scientific attention [1,2], in particular with respect to the opening of the South China Sea (SCS) [3,4]. One of the leading hypotheses about the opening of the SCS is that it was driven by forces related to the southward subduction of the proto-South China Sea (PSCS) crust [5,6]. Therefore, the PSCS is an important tectonic unit for understanding the tectonic evolution and geodynamic processes of the SCS as well as of SE Asia. Critical to the reconstruction of the Mesozoic geology of the SCS region, and more broadly of SE Asia, is the establishment of a precise temporal and spatial framework and evolution

path for the PSCS. However, this is complicated by the diverse array of Cenozoic tectonic processes (including rifting, subduction, terrane collision, and large-scale continental strike-slip faulting) with complex spatial and temporal patterns in the region, which have intensively modified the earlier geological characteristics of the PSCS [7]. Previous studies of the PSCS geology were based mainly on magmatic-sedimentary records from Borneo [8,9] and the Philippines [10], and the established view is that the oceanic lithosphere of the PSCS began to subduct during the Eocene on its southern side and was completely consumed during the early Miocene [11,12]. In contrast, the Mesozoic evolution of the northern side of the PSCS remains enigmatic owing to the lack of reliable geological records.

The onshore part of SE Asia, a major continental block that bounds the northern part of the SCS (Figure 1a), is characterized by widespread Mesozoic igneous rocks (Figure 1b) that can provide an important clue regarding the Mesozoic geodynamic mechanisms in the region. Despite extensive studies over the past 30 years, the Mesozoic geodynamic setting of South China remains hotly debated. The prevailing viewpoint considers that large-scale Mesozoic tectono-magmatic activities in South China were related to subduction of the paleo-Pacific plate [13,14]. However, the various proposed periods of time related to the initial subduction and rollback of the paleo-Pacific lithospheric slab [15,16] are excessively long and thus unlikely. Furthermore, metasomatism in South China, resulting from subduction of the paleo-Pacific plate beneath the Eurasian continent, was confined to the region east of the Wuyishan Range [17]. It has also been proposed that the tectonic pattern of the whole of South China during the Late Jurassic and Early Cretaceous was jointly controlled by the westward subduction of the paleo-Pacific plate and the northward subduction of the Neo-Tethys lithospheric plate [18]. Clearly, there is a range of views on the Mesozoic tectonic evolution of the northern SCS and the southeastern coastal region of China, meaning that the tectonic regimes and associated geodynamic processes, as well as the timings and spatial extents of influence of these regimes, have yet to be clearly understood.

Marine geophysics and numerical modeling have substantially improved our knowledge of the structure and tectonics of the SCS region [19,20]. Previous geophysical studies have inferred the presence of a buried Mesozoic subduction zone in the Northern SCS [21,22], but the tectonic attribute of the subducted slab is vague because no rock sample associated with a Mesozoic subduction event has been obtained to determine its geochemical affinity. However, some Mesozoic granitoid rocks have been dredged from the deep SCS basin [23] and have also been drilled from the northern shelf of the SCS [24]. The fresh rupture faces, angular shapes and the wide range of grain sizes of the dredged samples preclude long-distance fluvial or coastal transport, and the source rock must be situated in the slopes of the SCS, near continent–ocean transition (COT) [22,23]. These rocks contain strongly zoned plagioclase with sieve texture and partially resorbed biotite (± hornblende) [23,24]. The geochemical signatures of those rocks show negative Nb-Ta-Ti anomalies in trace element spidergrams [24], indicating that they were influenced by subducted components during their generation in a conceivable continental arc environment. However, the precise timing and geodynamic processes of subduction remain unresolved owing to a lack of proper petrologic evidence.

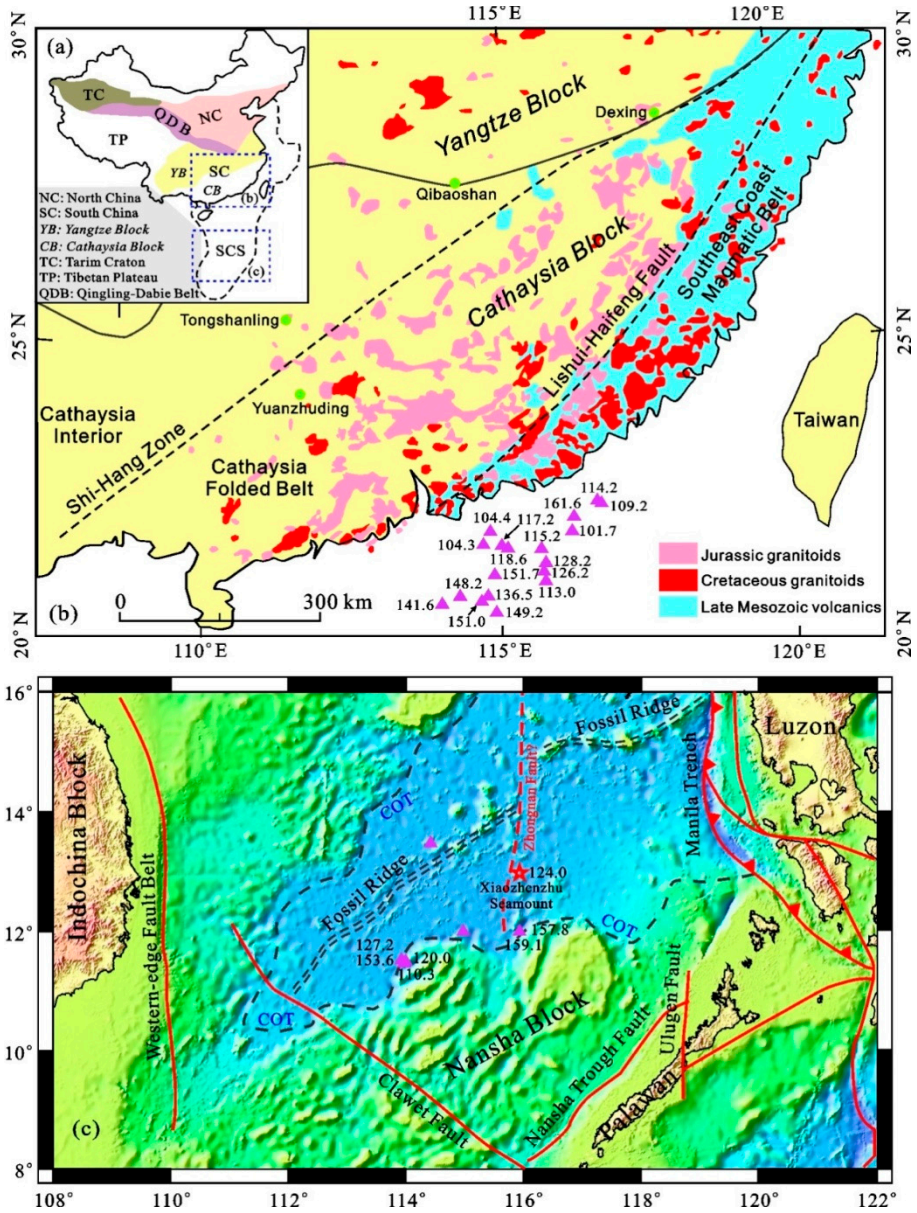



**Figure 1.** (**a**) Sketch tectonic map of China. (**b**) Simplified geological map showing the distribution of Mesozoic igneous rocks within the South China Block. The South China Block comprises the smaller Yangtze and Cathaysia blocks, with the Shi-Hang Zone and the Lishui-Haifeng Fault further dividing the Cathaysia Block into three tectonic units: the Cathaysia Interior, the Cathaysia Folded Belt, and the Southeast Coast Magmatic Belt. (**c**) Bathymetric map of the central-southern part of the SCS showing the sampling site (Xiaozhenzhu Seamount, red star) and age (Ma). The solid purple triangles and associated values indicate the locations and ages (Ma) of samples collected in previous studies [23–26].

Adakites are defined as andesitic-felsic igneous rocks characterized geochemically by high concentrations of $Al_2O_3$ (≥15 wt %), Sr (>400 μg/g), and light rare-earth elements (LREEs), and low concentrations of Y (≤18 μg/g) and heavy rare-earth elements (HREEs; e.g., Yb ≤ 1.9 μg/g), with high Sr/Y (>40) and La/Yb (>20) ratios [27,28]. Adakites also show a typical arc signature, namely depletions in Nb and Ta, and their origin is generally attributed to partial melting of subducted oceanic crust [29,30]. Adakites are not generally associated with mafic rocks. However, they are occasionally associated with high-Nb basalts (HNBs) or Nb-enriched basalts (NEBs). The adakite-HNB/NEB rock association has been viewed as a supporting argument for the slab-melting origin of adakites [31]. In the present study, we describe the first rock association of adakitic granodiorites with NEBs from

samples recovered from the Xiaozhenzhu Intraplate Seamount near the Zhongnan Fault of the SCS (Figure 1). The detailed petrography, geochemistry, Sr-Nd-Pb-Hf isotope composition, and zircon U-Pb and $^{40}Ar/^{39}Ar$ geochronology of these samples are examined to investigate their association and petrogenesis. In addition, we combine our petrologic data with other published data from the SCS to provide insights into the tectonic setting and geodynamic mechanisms of the study area during the Mesozoic.

## 2. Geological Background

The SCS basin is the largest and most complex, in structural terms, marginal sea of the Western Pacific. It is situated at the junction of the Eurasian, Pacific, and Indo-Australian lithospheric plates. The SCS basin is bordered by South China and the Indochina Peninsula to the north and west, respectively, and by the Luzon Island in the east and the Palawan Island in the south (Figure 1). The ages and orientations of magnetic lineations in the basin indicate that the SCS has undergone opening during the Oligocene and early Miocene [32,33]. As a result, several microblocks, including Dongsha (Pratas Islands), Nansha (Spratly Islands and the Dangerous Grounds), Xisha (Paracel Islands), Zhongsha (Macclesfield Bank), and Liyue (Reed Bank), were separated from South China, drifted southeastward, and finally collided with Borneo during the middle Miocene [5,33].

However, during the Mesozoic the modern SCS and the Philippines did not exist. Oceans surrounded the southeastern part of Eurasia, namely the paleo-Pacific Ocean to the east and the Tethys Ocean to the south [34]. To reconstruct the tectonic evolution of the SCS basin, the region where the SCS was formerly situated was inferred by [35] to have existed as an old marginal basin before it was subducted beneath Borneo. The existence of the presumable "paleo-South China Sea" basin was confirmed by the discovery of Mesozoic oceanic crust [36]. The palinspastic map of SE Asia shows that its oceanic crust formed during the Jurassic-Cretaceous (150–120 Ma), but that it subducted beneath Borneo during the Paleogene (60–40 Ma) as the SCS opened, about 20 Myr earlier than the timing inferred by [32]. Therefore, the term "paleo-South China Sea" was abandoned and subsequently replaced by "proto-South China Sea" in later studies [37,38].

The various microblocks of the SCS, including Dongsha, Nansha, Xisha, Zhongsha, Liyue, and Hainan Island, are considered to have been part of the late Paleozoic to middle Mesozoic continental basement [39,40]. Therefore, the Mesozoic marine strata distributed on these microblocks [41–43] must have recorded the geological history of the PSCS. In addition, Mesozoic magmatic rocks collected from the SCS [23,24] and from the adjacent Hainan Island and the Vietnamese Nhatrang-Dalat area [44] preserve a record of information regarding the tectonic evolution of the PSCS. Nevertheless, the tectono-geological evolution of the PSCS is based mainly on the geological formations in and around Borneo [11], including the following: (1) the ophiolitic basement, probably mainly of Cretaceous age in North and East Borneo; (2) the associated high-pressure (HP) and low-temperature (LT) metamorphic rocks, recording Cretaceous subduction beneath Borneo; (3) dioritic and granitic rocks that could represent arc plutonic intrusions within an older ophiolitic basement; (4) the Rajang Group flysch-belt (Paleogene turbidites, olistostromes, and assemblages of generally deep-water origin), which may be interpreted as a north-facing accretionary prism; and (5) the Crocker Formation (Miocene shallow-water sediments) that is unconformably overlying the older accretionary complex rocks and accreted continuously farther north until later in the Miocene.

At present, the key features of the PSCS are that it formerly occupied the area south of Indochina and South China, its oceanic crust is Mesozoic in age, and it was completely eliminated by subduction on its southern side from the Eocene to the early Miocene. The subduction zone is known to have extended as far west as offshore Sarawak. The PSCS narrowed towards the west, and its western end met the Sunda Shelf in a zone of dextral strike-slip faulting. The south-dipping subduction was terminated by collision between the continental crust of South China and a volcanic arc extending from Sabah to the Cagayan Ridge [6]. However, the geotectonic environment of the PSCS continues to be a subject of controversy. The main viewpoints are that the PSCS was (1) a gulf of the paleo-Pacific that

developed during the Mid-Triassic to Cretaceous [32], (2) one of the back-arc basins (BAB) derived from the northward subduction of the paleo-Pacific plate [45], (3) part of the Meso-Tethys or an extension of the main Tethys to the east [46], or (4) a northeastern marginal sea of the Tethys bordered by the South China Block [44].

## 3. Samples and Analytical Methods

### *3.1. Sample Descriptions*

The granodiorite and NEB samples examined in this study were dredged during the 2015 R/V Haiyang 4 cruise organized by the Guangzhou Marine Geological Survey (GMGS) (Guangzhou, China). The investigated rock specimens were collected from the Xiaozhenzhu Seamount (location: 12°42′57.03″ N, 115°55′53.89″ E; water depth: ~4043 m) near the Zhongnan fault zone of the southern SCS (Figure 1c). Two pieces of granodiorites, two pieces of NEBs, and a few sedimentary rock samples of a total weight of ~100 kg were obtained by dredging. The granodiorite and NEB samples were covered by a thin (~1–2 cm) layer of Fe-Mn–rich crust (Figure 2a,b).

The granodiorites show a fine- to medium-grained (0.5–4.0 mm) inequigranular texture (Figure 2c). The main minerals of the granodiorites were plagioclase, quartz, biotite, and K-feldspar. Plagioclase (~60 vol %), with crystal sizes of up to 4 mm in length, appeared as euhedral crystals some of which are zoned. The plagioclase crystals were commonly partly altered to sericite. Quartz (20–25 vol %) occurred as anhedral crystals. Biotite (8–10 vol %) appeared as lath-shaped crystals with varying size (0.5–3.0 mm) and was pleochroic from beige to dark brown, with some crystals being altered to chlorite. Potassium-feldspar crystals (approximately 7 vol %) in all cases displayed microcline twinning, and some parts of them were altered to chlorite or sericite. Accessory minerals included sphene, apatite, zircon, magnetite, and allanite.

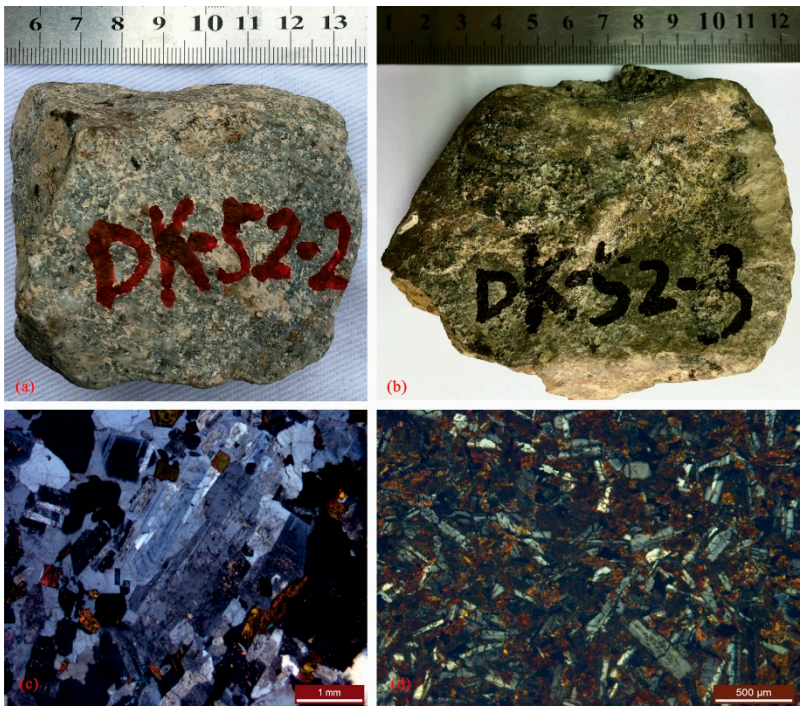



**Figure 2.** Photographs of granodiorite (**a**) and Nb-enriched basalt (NEB) (**b**) and photomicrographs (cross-polarized nicols) of granodiorite (**c**) and NEB (**d**).

The NEB samples were porphyritic with large euhedral plagioclase phenocrysts (Figure 2d) and had an intergranular texture and a massive structure. Their glassy groundmass contained plagioclase

laths (≤0.5 mm) and fine-grained interstitial clinopyroxene (≤0.3 mm) and accessory magnetite. Most of the clinopyroxene grains were altered to tremolitic amphibole.

### *3.2. Zircon U-Pb Dating and Hf Isotope Analysis*

Zircons from the granodiorite sample DK-52-2 were concentrated using conventional heavy liquid and magnetic separation techniques and handpicked under a binocular microscope at the Guangzhou Institute of Geochemistry, Chinese Academy of Sciences (GIG-CAS), Guangzhou, China. More than 300 zircon grains were randomly selected, mounted in epoxy resin and polished to approximately half their thickness. Their internal morphology was examined by conventional optical microscopy and cathodoluminescence (CL) imaging using a JEOL JXA-8230 electron probe microanalyzer (EPMA) to ensure that the zircons selected for analysis were the least fractured and free of any mineral inclusions.

Zircon U-Pb dating was performed using a laser ablation inductively coupled plasma mass spectrometer (LA-ICP-MS) at the State Key Laboratory of Isotope Geochemistry, GIG-CAS, China. Uranium-Pb isotope analysis was performed using an Agilent 7500a ICP-MS coupled with a Resonetic Resolution M-50 ArF Excimer laser source ($\lambda$ = 193 nm). The analytical conditions were: laser energy of 80 mJ, repetition rate of 10 Hz, and spot diameter of 31 μm, with each analysis including a background gathering of around 20 s and an interval of 50 s of data acquisition from the samples. Helium was used as a carrier gas to take ablated aerosols to the ICP source. The standards NIST 610, TEM, and 91500 were used as external calibration standards for determining the elemental fractionation and U-Pb age, and $^{29}$Si was used as an internal standard. The off-line selection and integration of background and analytical signals, time-drift correction, and quantitative calibration for U-Pb dating were performed using ICPMSDataCal [47,48]. Concordia diagrams and weighted mean ages were obtained using Isoplot 3.70 [49].

The in situ Hf isotope compositions of zircons subjected to U-Pb dating were determined using a multi-collector-ICP-MS (MC-ICP-MS, Neptune Plus) equipped with a Resonetic Resolution M-50 ArF 193 nm excimer laser ablation system at the State Key Laboratory of Isotope Geochemistry, GIG-CAS, China. This system allows quick responses to be made to changes in sample or ablation conditions (a 99% signal washout in less than 1.5 s) by use of an innovative sample cell design. An energy intensity on target of ~5 J/cm$^2$ was used during analysis, with helium gas mixed with argon (and nitrogen as an additional di-atomic gas to enhance sensitivity) being used as a carrier to take ablated sample aerosols from the sample cell into the MC-ICP-MS torch for analysis. A spot size of 44 μm and a repetition rate of 5 Hz were used for all analyses. The standard 91500 was analyzed twice every 10 analyses. The interference of $^{176}$Yb on $^{176}$Hf was corrected using $^{176}$Yb/$^{173}$Yb = 0.7876. The minor interference of $^{176}$Lu on $^{176}$Hf was corrected using $^{176}$Lu/$^{175}$Lu = 0.02656. The values of initial Hf isotope and $^{176}$Hf/$^{177}$Hf ratios were calculated using the $^{176}$Lu decay constant of $1.865 \times 10^{-11}$ and the measured $^{176}$Lu/$^{177}$Hf ratios. Two-stage Hf model ages ($T_{DM2}$) were calculated by assuming a $^{176}$Lu/$^{177}$Hf ratio of 0.015 for average continental crust [50].

### *3.3. $^{40}$Ar/$^{39}$Ar Dating*

Whole-rock incremental-heating $^{40}$Ar/$^{39}$Ar dating of the NEB was performed at the State Key Laboratory of Isotope Geochemistry, GIG-CAS, China. Sample DK-52-3 was selected for $^{40}$Ar/$^{39}$Ar dating and was first crushed to grains of a size of 1–2 mm. The grains were sonicated in 1 N $HNO_3$ for 60 min and in 3.5 N HCl for an additional 60 min; then sequentially rinsed (10 min) in acetone, deionized water, and ethanol; and then air-dried. Five to six of the freshest and most equant whole-rock grains were handpicked under a binocular microscope and carefully loaded into Al irradiation disks together with the monitor standard ZBH-2506 biotite. Each disk was wrapped in aluminum foil, vacuum sealed in a quartz vial, and then irradiated for 54 h in the 49-2 reactor at the Institute of Atomic Energy, Beijing, China. After a decay period, three grains were incrementally heated using a COHERENT-50W $CO_2$ continuous laser beam. The released gases were purified by two Zr/Al getter pumps operated for 5–8 min at room temperature and ~450 °C, respectively. The background of the

sample holder was lower than 2 mV pre experiment and 4–6 mV during the experiment after a 5 min evacuation, and the signal of the sample was controlled within the range of 40–200 mV.

The $^{40}Ar/^{39}Ar$ dating was performed using a GV5400 MS. The *J*-values for the samples were determined using ZBH-2506 biotite (132.5 Ma) as a flux monitor. To obtain *J*-values for unknown samples, the ZBH-2506 was packed between every four samples in quartz tubes with each tube containing four packets of ZBH-2506. Based on the *J*-values and the positions of ZBH-2506 in the sample tube, a regression line was obtained for each sample tube with the *J*-values for the unknown samples being calculated by interpolation using the regression line. A *J*-value uncertainty of 0.15% (1σ) was considered in the reported ages. The $^{40}Ar/^{39}Ar$ dating results were calculated and plotted using ArArCALC software [51]. The data were corrected for atmospheric contamination, nucleogenic interference, and mass discrimination. An $^{40}Ar/^{36}Ar$ value of 298.56 ± 0.31 for atmospheric Ar [52] was used for calculating the discrimination of the MS. The $^{40}Ar/^{39}Ar$ ages are reported using currently accepted decay constants [53]. The errors include those produced in the irradiation correction factors and in *J*, but do not include the uncertainty in the age of the flux monitor or the uncertainty in the K decay constants.

### *3.4. Whole-Rock Major and Trace Element Analysis*

Samples for whole-rock geochemical analysis were sawn into chips (~5 mm in thickness) and washed once with tap water and then twice with deionized water. After drying, the less weathered parts of each sample were selected and crushed. The grains were washed successively with tap water, 2% HCl, and deionized water. Finally, the grains were powdered to <200 mesh using an agate mortar. Whole-rock major element contents were determined at the State Key Laboratory of Isotope Geochemistry, GIC-CAS, China. The loss on ignition (LOI) of sample powders was determined at a temperature of 1000 °C. Whole-rock sample powders were then fluxed with $Li_2B_4O_7$ (1:8) at 1150–1200 °C to make homogeneous glass discs using an Analymate Company V8C automatic fusion machine. The measurements were performed using X-ray fluorescence (XRF) spectrometry with a Rigaku 100e instrument. The analytical precision was better than 1%, as assessed by monitoring the standards GSR-3 and BHVO-2 [54].

Trace element analyses of bulk-rock samples were conducted using an ICP-MS (Thermo X Series II) at the Radiogenic Isotope Facility, School of Earth and Environmental Sciences, the University of Queensland (SEES-UQ), Brisbane, Australia. Approximately 35 mg of sample powder was precisely weighed and first digested with a distilled mixture of HF-$HNO_3$ (4:1) in Savillex$^{TM}$ Teflon beakers at 110 °C for 24 h. Then the solutions were heated at 120 °C to incipient dryness. A mixture of HF-$HNO_3$ was again placed into the beakers and dissolution was maintained in an oven at 195 °C for 2 days. The solutions were then dried to evaporate HF. The sample residues were re-dissolved with concentrated $HNO_3$, followed by 1:1 $HNO_3$, and dried again. Finally, the sample residues were dissolved in 8 mL of 5% $HNO_3$ stock solution. A weighted aliquot of this stock solution, corresponding to ~2 mg of the original powder, was mixed with an internal standard containing $^{6}Li$, $^{61}Ni$, $^{103}Rh$, $^{115}In$, $^{187}Re$, and $^{235}U$ spikes and diluted with 2% $HNO_3$ to achieve a final dilution factor of about 1:5000 for trace element analyses. The standards BHVO-2, W-2, and JCP-1 were used as calibration standards and were cross-checked with BIR-1. Instrumental drift in mass response was corrected with both the multi-element internal standard and an external drift monitor. The average full procedural blank values of this study were less than 1 pg for high field strength elements (HFSEs) and REEs and 100 pg for large-ion lithophile elements (LILEs).

### *3.5. Bulk-Rock Sr-Nd-Pb Isotope Analysis*

Strontium-Nd-Pb isotope ratios of whole-rock samples were measured using an MC-ICP-MS (Nu Plasma HR) at the Radiogenic Isotope Facility, SEES-UQ, Brisbane, Australia. Approximately 200 mg of powder for each sample was leached ultrasonically in 4 mL of 4 N HCl at 50 °C for 20 min. Each leached sample was then dissolved in a 20 mL Teflon beaker by adding 1 mL of $HNO_3$ and 3 mL of

HF and placed on a hotplate at 80 °C overnight. Then the lid was closed, and the temperature was increased to 140 °C, after which the samples were checked to ensure that they were fully dissolved. The sample solutions were then dried at 80 °C. One milliliter of concentrated $HNO_3$ was added to each beaker, and the solution was dried again at 80 °C. Afterwards, 10 mL of acid mixture consisting of 1 N HCl and 0.25 N $HNO_3$ was added to the sample residues and heated on a hotplate overnight at 90 °C with the lids tightly closed. This stage ensured the complete removal of fluorides. After the sample solutions had been evaporated on a hotplate to their original dryness, 1 mL of 7 N $HNO_3$ was added and the solutions were dried to convert fully to nitrites. After evaporation to dryness on a hotplate, 2 mL of 1 N $HNO_3$ was added to dissolve the residues at 80 °C with the lids tightly closed.

Purification and elution of Sr, Nd, and Pb were performed following a continuous column chemistry procedure using Sr-Spec, TRU-Spec, and Ln-Spec resins. Strontium and Pb were separated from matrices and interference elements and purified using Sr-Spec resin. When Sr isotope ratios were measured, the NBS-987 standard was used to monitor the detector efficiency drift of the instrument, and $^{86}Sr/^{88}Sr = 0.1194$ was used for exponential mass fractionation corrections. The deviation of the repeatedly measured mean value (0.710236 ± 8, 2σ) from the laboratory's previously obtained long-term average of 0.710239 ± 5 (2σ) was used to correct for all samples. Lead isotopes were analyzed together with a Tl spike ($^{203}Tl$-$^{205}Tl$ isotopes) to correct for mass-dependent isotope fractionation. The entire procedure was monitored using standard SRM-981. BCR-2 was analyzed as an external standard to evaluate the accuracy and precision. Neodymium was further separated using TRU-Spec and Ln-Spec resins. Neodymium isotopes were analyzed automatically using a three-sequence dynamic procedure. Instrumental bias and mass fractionation were corrected by normalizing raw ratios to $^{146}Nd/^{144}Nd = 0.7219$. The $^{143}Nd/^{144}Nd$ data are presented relative to an Ames Nd metal $^{143}Nd/^{144}Nd$ value of 0.511966. Accuracy was assessed by analyzing the JNdi-1 standard and the USGS BHVO-2 rock standard. Procedural blanks were <1 ng for Sr, <100 pg for Pb, and <25 pg for Nd.

## 4. Results

All the analytical data are provided as Supplementary Materials (Tables S1–S5). For the purpose of comparison, we have compiled the published data for isotope ages, major and trace elements, and Sr-Nd-Pb isotopes of granitoid rocks from the SCS. These published data are also listed in the Supplementary Tables S4 (isotope ages, major and trace elements) and S5 (Sr-Nd-Pb isotopes) and plotted in relevant diagrams together with our data.

### *4.1. Zircon U-Pb Ages and Hf Isotope Compositions of the Granodiorite*

Zircon grains selected for U-Pb dating were prismatic, colorless, and transparent, with lengths of ~100–300 μm and length-to-width ratios varying from 2:1 to 4:1. Cathodoluminescence images show that the zircon grains have clear microscale oscillatory zoning with well-developed pyramidal faces (Figure 3), suggesting a magmatic origin. The results of zircon LA-ICP-MS U-Pb dating of the granodiorite are listed in the Supplementary Table S1 and are displayed graphically in Figure 4a. All analyses have variable U (113–1209 μg/g) and Th (70–1195 μg/g) concentrations and high Th/U ratios (0.23–1.69). These Th/U ratios are consistent with those of magmatic zircons and distinctly higher than those of metamorphic zircons, which generally have Th/U ratios of <0.1 [55]. Of the analyses, 59 are concordia (with the exception of spots 18, 20, 22, 32, 40, and 41) and yield a weighted $^{206}Pb/^{238}U$ mean age of 124.0 ± 0.3 Ma, indicating crystallization of the granodiorite during the Early Cretaceous (Aptian). In addition, spot 20 has a $^{207}Pb/^{206}Pb$ age of 1700 Ma, significantly different from the others (Supplementary Table S1), probably implying that the source region for the granodiorite contained zircons that were formed during the Paleoproterozoic Era.

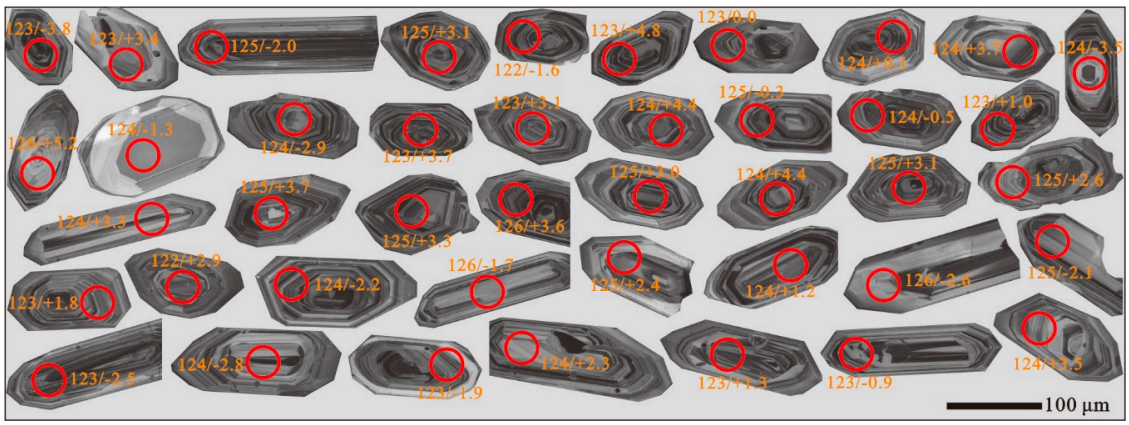



**Figure 3.** Cathodoluminescence images of representative zircons for in situ analyses of U-Pb and Hf isotopes. Numbers next to analysis spots (red circles) are U-Pb ages (Ma)/$\varepsilon_{Hf}(t)$ values.

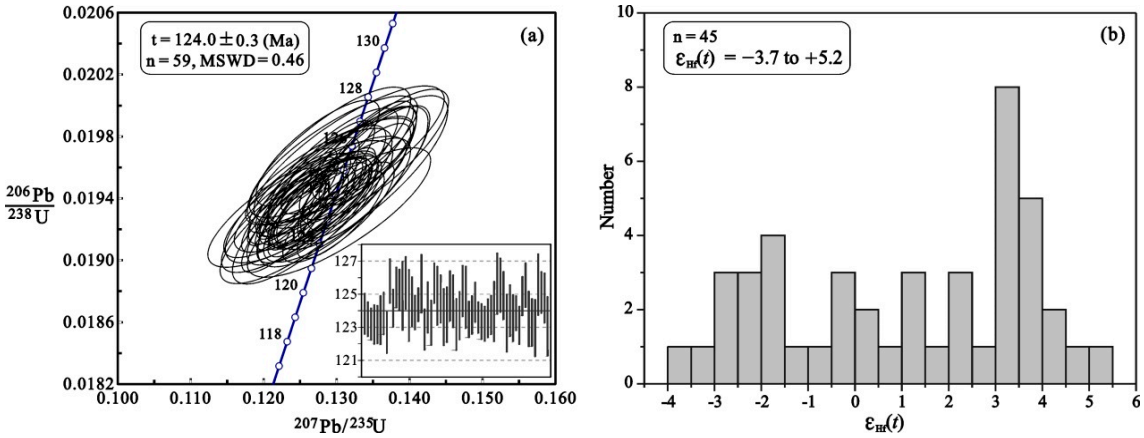



**Figure 4.** Zircon U-Pb concordia diagram and $^{206}Pb/^{238}U$ weighted mean ages (**a**) and probability histogram of $\varepsilon_{Hf}(t)$ values (**b**) for the granodiorite.

In situ zircon Hf isotope compositions were determined for 45 zircon grains, using the same sites as for LA-ICP-MS U-Pb dating, and the results are given in the Supplementary Table S2. All analyzed zircons from the granodiorite have relatively low $^{176}Yb/^{177}Hf$ (0.014440–0.056857) and $^{176}Lu/^{177}Hf$ (0.000531–0.001735) ratios. The $^{176}Hf/^{177}Hf$ ratios range from 0.282593 to 0.282842, with $\varepsilon_{Hf}(t)$ values spanning a wide range from −3.8 to +5.2 (average of +1.0) (Figure 4b). The zircons yield relatively young model ages ($T_{DM1}$ = 942–579 Ma and $T_{DM2}$ = 1415–851 Ma).

### *4.2. $^{40}Ar/^{39}Ar$ Ages of the NEB*

NEB sample DK-52-3 was selected for $^{40}Ar/^{39}Ar$ dating. The $^{40}Ar/^{39}Ar$ age results (including 1σ uncertainties) are reported in the Supplementary Table S3 and are displayed in age plateau and normal isochron diagrams in Figure 5a,b, respectively. The NEB yields a whole-rock weighted plateau age of 124.0 ± 0.8 Ma (mean square weighted deviation or MSWD = 0.82) with 59.64% released gas in the 6th to 10th stages (Figure 5a), which is within error of the total fusion age of 125.2 ± 0.7. These data give an isochron age of 119.7 ± 5.7 Ma with an initial $^{40}Ar/^{36}Ar$ value of 311.4 ± 15.5, close to the atmospheric value (295.5), and an inverse isochron age of 118.4 ± 5.9 Ma with an initial $^{40}Ar/^{36}Ar$ value of 315.3 ± 18.1. We note that the whole-rock $^{40}Ar/^{39}Ar$ age spectra show high apparent ages and increasing K/Ca ratios at low-temperature heating increments (Figure 5a), possibly reflecting submarine alteration of the sample.

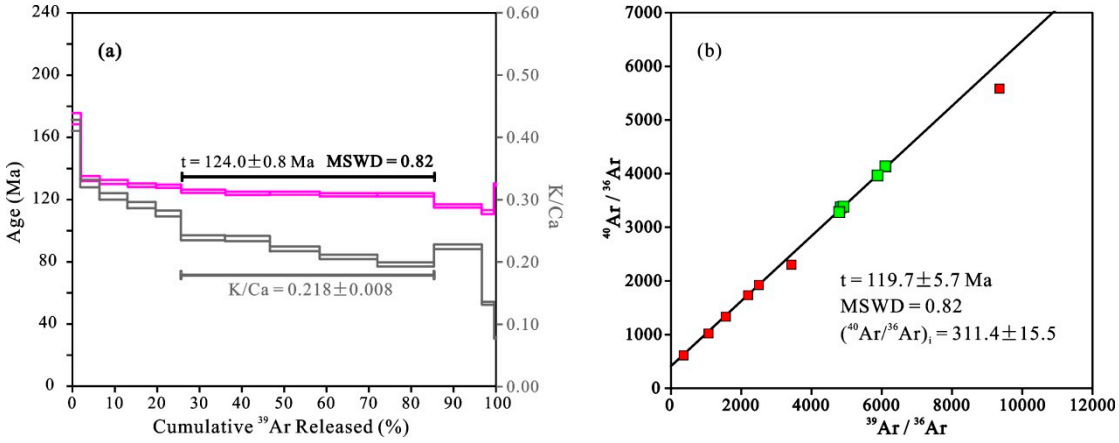



**Figure 5.** $^{40}$Ar/$^{39}$Ar plateau age and K/Ca ratio spectra (**a**) and $^{40}$Ar/$^{36}$Ar versus $^{39}$Ar/$^{36}$Ar diagram (**b**) for whole-rock NEB samples. Age uncertainties correspond to the 1σ level. On the isochron plot, green squares represent the data used to determine the isochron.

### 4.3. Geochemistry

The sampled SCS granodiorites show consistent whole-rock chemical compositions. The granodiorites are characterized by felsic compositions ($SiO_2$ = 67.40–67.63 wt %) and high $Al_2O_3$ (15.44–15.50 wt %), with a $Mg^{\#}$ {$Mg^{\#}$ = 100 × Mg/(Mg + Fe)} ratio range of 46.83–47.18 (Supplementary Table S4). These rocks have a calc-alkaline composition in a $Zr/TiO_2$ versus $SiO_2$ diagram (Figure 6a). The granodiorites also have high total alkali ($Na_2O$ + $K_2O$) contents of 6.89–6.98 wt % and have near-equal $Na_2O$ and $K_2O$ contents and relatively high $K_2O/Na_2O$ ratios (0.92–0.95), permitting their classification as high-K calc-alkaline series rocks (Figure 6b).

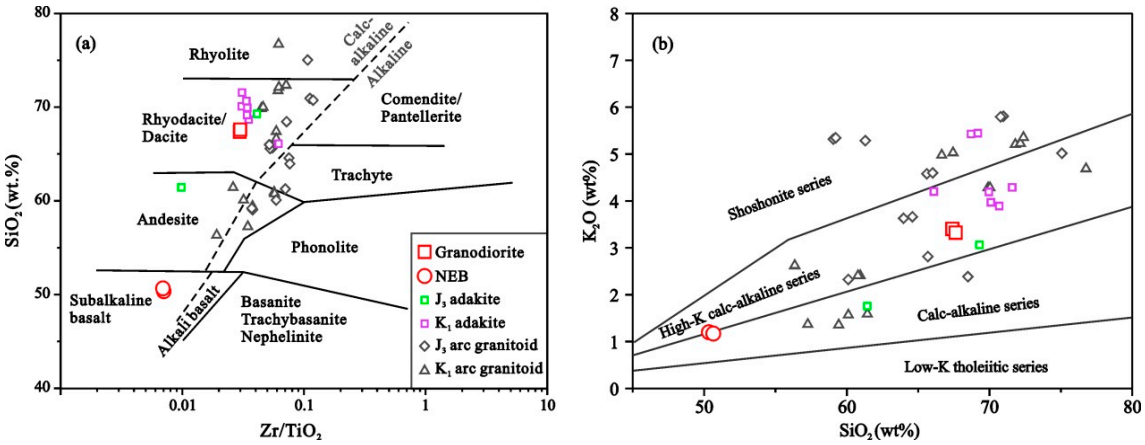



**Figure 6.** Classification diagrams of $SiO_2$ versus $Zr/TiO_2$ (**a**) and $K_2O$ versus $SiO_2$ (**b**) for the granodiorite and NEB samples obtained from the Xiaozhenzhu Seamount near the Zhongnan Fault in the South China Sea (SCS). The compositions of the Late Jurassic ($J_3$) adakites and arc granitoids and of the Early Cretaceous ($K_1$) adakites and arc granitoids from the SCS [23,24] are also shown.

The granodiorites have low total REE concentrations (84.7–91.6 μg/g). Chondrite-normalized REE patterns (Figure 7a) show negligible to weak negative Eu anomalies ($\delta_{Eu}$ = 0.88–0.93) and are enriched in LREEs and depleted in HREEs with high $(La/Yb)_N$ ratios (13.8–15.7). Their low concentrations of Yb and Y (Yb = 0.93 μg/g, Y = 9.78 μg/g, averages of two samples; Supplementary Table S4), together with their relatively high Sr contents (351 μg/g, average of two samples; Supplementary Table S4) and Sr/Y ratios (34.73–36.98) lead to their classification as adakites (Figure 8a,b). In addition, these rocks show strong enrichment in LILEs relative to HFSEs and pronounced negative Nb-Ta-Ti anomalies in primitive mantle

(PM)-normalized incompatible element spidergrams (Figure 7b), implying that subduction-related volatile materials were added to their parental magmas. A Ta versus Yb discrimination diagram (Figure 9a) further demonstrates that these granodiorites were formed in a volcanic arc setting.

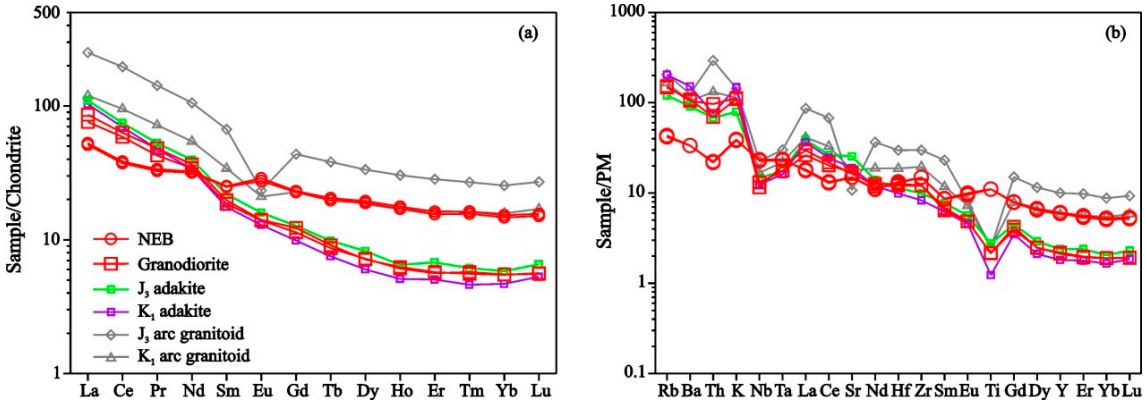



**Figure 7.** Chondrite-normalized rare-earth element patterns (**a**) and primitive mantle (PM)-normalized trace element spidergrams (**b**) of adakitic granodiorites and NEBs from the Xiaozhenzhu Seamount near the Zhongnan Fault in the SCS. The averaged compositions of the Late Jurassic ($J_3$) adakites (average of 2 samples) and arc granitoids (average of 13 samples) and of the Early Cretaceous ($K_1$) adakites (average of 7 samples) and arc granitoids (average of 16 samples) from the SCS [23,24] are also shown for comparison. The normalizing values are from [55].

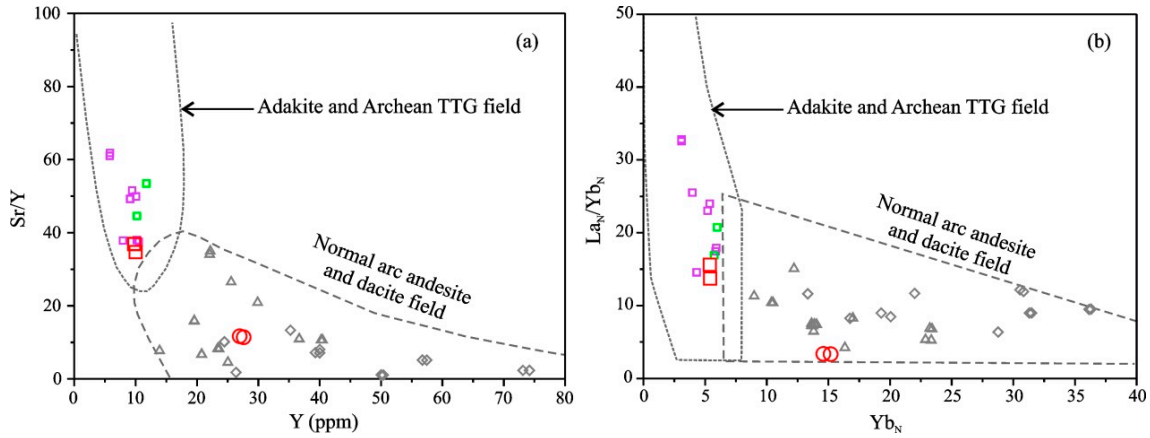



**Figure 8.** Plots of Sr/Y versus Y (**a**) and $La_N/Yb_N$ versus $Yb_N$ (**b**) for the granodiorites and NEBs from the Xiaozhenzhu Seamount near the Zhongnan Fault in the SCS. Also shown are the data of Mesozoic arc and adakitic granitoids from the SCS [23,24]. The fields of adakite and Archean TTG, and of normal arc andesite and dacite are from [56] and [57], respectively. The symbols are as in Figure 6.

The investigated NEBs possess unsaturated $SiO_2$ contents (50.34–50.65 wt %) and high $Al_2O_3$ (15.27–15.32 wt %), CaO (6.15–6.27 wt %), and total Fe ($Fe_2O_3{}^T$ = 12.09–12.21 wt %) contents (Supplementary Table S4). These rocks are classified as subalkaline basalts in a $Zr/TiO_2$ versus $SiO_2$ diagram (Figure 6a). They are Na-rich ($Na_2O/K_2O$ = 2.98–3.08), and their compositions are transitional between those of medium- and high-K calc-alkaline series (Figure 6b). The NEB samples are also rich in $TiO_2$ (2.34–2.38 wt %), $P_2O_5$ (0.20–0.23 wt %), Zr (166–167 μg/g), and Nb (16.2–16.7 μg/g) contents and have high $(Nb/Th)_{PM}$ (1.02–1.08) and $(Nb/La)_{PM}$ (1.25–1.33) ratios. In chondrite-normalized REE patterns, the investigated NEB samples display LREE enrichments ($(La/Yb)_N$ = 3.45–3.49) and weak positive Eu anomalies ($\delta_{Eu}$ = 1.16–1.20) consistent with the fractionation of plagioclase (Figure 7a). Although they are enriched in LILEs relative to HFSEs, the NEBs display a lower degree of enrichment than the associated granodiorites (Figure 7b). In addition, as with ocean island basalts (OIBs), the NEBs

do not exhibit negative Nb-Ta-Ti anomalies in PM-normalized incompatible element spidergrams. In the Th/Yb versus Ta/Yb diagram (Figure 9b), the investigated NEBs plot on the edge of the compositional field for volcanic rocks that have an active continental margin origin.

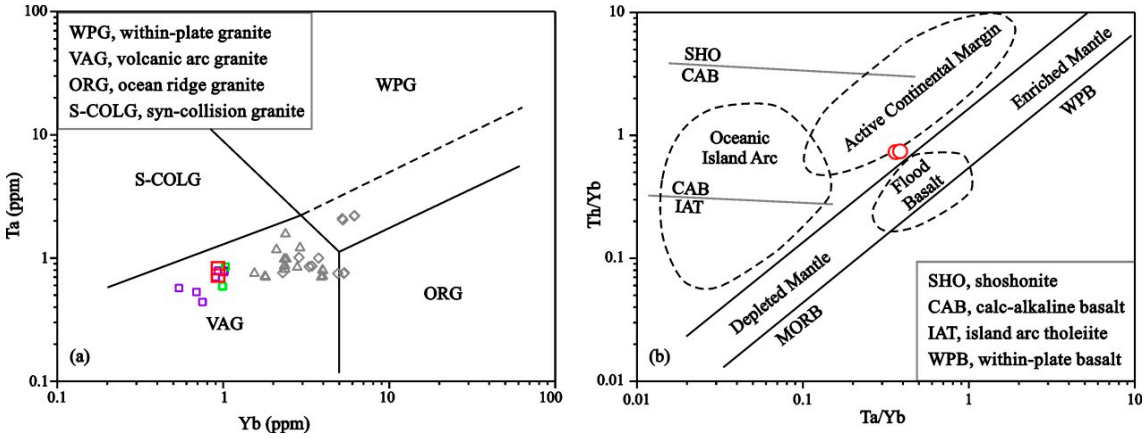



**Figure 9.** (**a**) Ta versus Yb discrimination diagram [58] for the SCS granodiorites of the present study and Mesozoic arc and adakitic granitoids from the South China Sea [23,24]. The symbols are as in Figure 6. (**b**) Th/Yb versus Ta/Yb diagram [59] for the NEBs sampled from the Xiaozhenzhu Seamount near the Zhongnan Fault in the SCS.

### *4.4. Whole-Rock Sr-Nd-Pb Isotope Geochemistry*

The Sr-Nd-Pb isotope compositions of the granodiorites and NEBs are presented in the Supplementary Table S5 and Figure 10. The granodiorites have homogeneous and relatively depleted Sr-Nd isotope compositions, with $^{87}Sr/^{86}Sr$ and $^{143}Nd/^{144}Nd$ ratios of 0.706792–0.706797 and 0.512381–0.512386, respectively. Their $\varepsilon_{Nd}(t)$ values are high with respect to those of the Cretaceous adakites in the Lower Yangtze River Belt, varying from −3.52 to −3.61 (Figure 10a). They also have corresponding Mesoproterozoic $T_{DM2}$ model ages (1.123–1.112 Ga) that are identical to the zircon Hf isotope model ages. In addition, the Sr-Nd isotope compositions of the granodiorites are clearly different from those of the Cenozoic adakites derived from subducted oceanic crust around the Pacific (Figure 10a). The investigated NEBs have $^{87}Sr/^{86}Sr$ ratios of 0.703837–0.703841 and $^{143}Nd/^{144}Nd$ ratios of 0.512755–0.512756. The $\varepsilon_{Nd}(t)$ values of the NEBs span a narrow range from +2.90 to +2.93 and plot close to the edge of the Indian Ridge MORB field, being lower than those of the East Pacific Rise and SCS MORB, with corresponding Mesoproterozoic $T_{DM2}$ model ages (1.055–1.077 Ga) similar to those of the granodiorites they are associated with.

In spite of their contrasting Sr-Nd isotopic compositions, the granodiorites and the NEBs have similarly enriched Pb isotope compositions (Figure 10b). The granodiorites yielded $^{206}Pb/^{204}Pb$ = 18.7711–18.7813, $^{207}Pb/^{204}Pb$ = 15.6444–15.6448, and $^{208}Pb/^{204}Pb$ = 38.8909–38.8912, and the NEBs yielded $^{206}Pb/^{204}Pb$ = 19.1471–19.1477, $^{207}Pb/^{204}Pb$ = 15.6727–15.6631, and $^{208}Pb/^{204}Pb$ = 39.2664–39.2669, indicating that the NEBs are more enriched than the granodiorites. In addition, all the investigated rock samples plot to the left of the Northern Hemisphere reference line (NHRL) in Figure 10b. All the studied rocks plot in the field of the Indian Ridge (IR) MORB (Figure 10b).

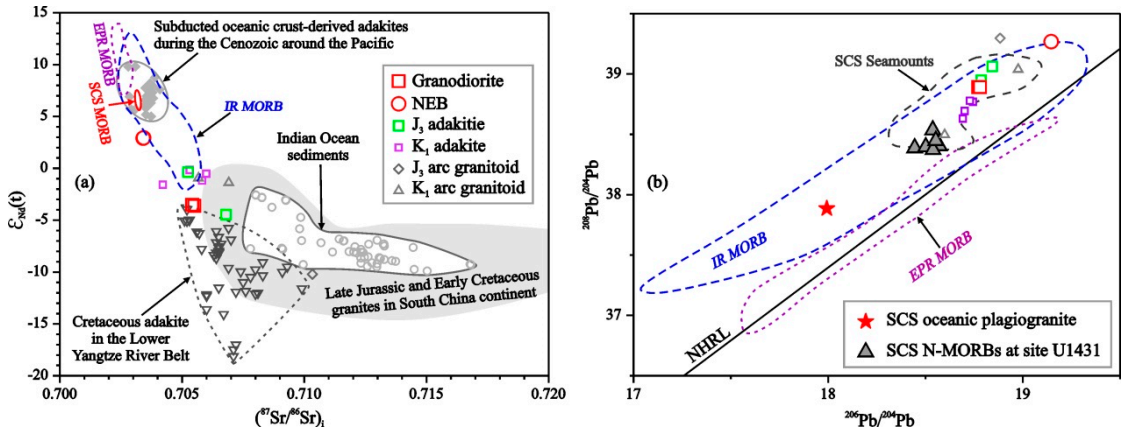



**Figure 10.** (**a**) $\varepsilon_{Nd}(t)$ versus initial $^{87}Sr/^{86}Sr$ and (**b**) $^{208}Pb/^{204}Pb$ versus $^{206}Pb/^{204}Pb$ diagrams for the granodiorites and NEBs from the Xiaozhenzhu Seamount near the Zhongnan Fault in the SCS. The sources of data for comparison with the data of the present study are as follows: Mesozoic arc and adakitic granitoids from the SCS [23,60,61]; Late Jurassic and Early Cretaceous granites in South China continent [62]; SCS oceanic plagiogranite [63]; the East Pacific Rise (EPR), SCS, and Indian Ridge (IR) MORB [64]; Cretaceous adakites in the Lower Yangtze River Belt [65]; oceanic-crust-derived adakites subducted around the Pacific during the Cenozoic [66–68]; and Indian Ocean sediments [69–71].

## 5. Discussion

### 5.1. Relationship between Granodiorites and Nb-Enriched Basalts

In this study, granodiorites and basalts were sampled together for the first time from the same seamount within the SCS basin. Zircon U-Pb dating indicates that granodiorites crystallized during the Early Cretaceous (124.0 ± 0.3 Ma) (Figure 4a). In addition, whole-rock $^{40}Ar/^{39}Ar$ dating demonstrates that basalts were erupted at almost the same time, during the Early Cretaceous (124.0 ± 0.8 Ma) (Figure 5a). These age results show that the investigated rocks have near-identical formation ages, suggesting a cogenetic relationship. Granodiorites have high $Al_2O_3$, Sr, and LREE contents and low Y and HREE contents, with correspondingly high Sr/Y and La/Yb ratios. These features are identical to those of adakites, indicating that the investigated granodiorites are adakitic in composition. The studied basalts are characterized by high Nb concentrations. These rocks are classified as NEBs. In general, adakites are not associated with other mafic rocks besides NEBs or HNBs [31,72]. Associations of adakites with NEBs of various ages (Early Paleozoic to Cenozoic) have been reported from different regions, including (but not limited to): Panama and Costa Rica [66], Northern Baja California [68], Cascades [73], and Kamchatka [74]. Collectively, the spatial, temporal and geochemical relationships between the granodiorite and basalt samples collected from the Xiaozhenzhu Seamount (near the Zhongnan Fault) in the SCS represent an association of rocks that share a common petrogenetic history.

### 5.2. Tectonic Setting

The SCS comprises three tectonic units: the deep basin and the conjugate northern and southern continental margins. The geotectonic evolution of the SCS during the Cenozoic has been thoroughly studied, and a common consensus on the tectonic setting of the continental margins of the SCS has been inferred; that is, the SCS margins were passive and evolved from continental rifting to seafloor spreading in the early Cenozoic [75]. Considering that subduction of the paleo-Pacific plate beneath the South China Block started around the Early-Middle Jurassic (~180 Ma); [36,76] and that the Late Mesozoic granitic-volcanic rocks become younger toward the coast, most researchers consider that the SE Asian continental margin during the Mesozoic was an active continental margin related to subduction of the paleo-Pacific plate [77]. On the contrary, a Mesozoic volcanic arc in the northern SCS margin has been inferred on the basis of geophysical data [22,78].

Herein, we bring together data from more than 40 Mesozoic granitoid rocks and two NEBs dredged or drilled from the SCS (including samples from the present study and data obtained from previous research) to constrain the geotectonic setting of the SE Asian continental margin. These granitoid rocks are characterized by $SiO_2$ contents varying from 56.34 wt % to 76.76 wt % and are classified as intermediate to felsic I-type granitoids [23,24]. Most of the Mesozoic granitoid rocks have high $K_2O$ contents and are mainly classified as high-K calc-alkaline rocks (Figure 6b), which are generated at active continental margins [79]. In Figure 9a, most of the Mesozoic granitoid rocks plot in the field of volcanic arc granites, also supporting an arc setting. More importantly, the granitoid rocks show noticeable depletions of Ta, Nb, and Ti in PM-normalized incompatible element patterns (Figure 7b). These depletions might have been produced by fractionation of titanite and/or rutile from the parental magmas of the granitoids. However, fractionation of titanite and/or rutile would not only lead to negative anomalies in Nb, Ta, and Ti but would also result in apparent depletions in Zr and Hf and an increase in the Nb/Ta ratio [80]. This is inconsistent with the absence of Zr and Hf anomalies in the investigated rocks (Figure 7b). However, minor fractionation of rutile cannot be entirely excluded as it can explain the small decoupling between Nb and Ta (Figure 7b). Therefore, the Nb, Ta, and Ti depletions recorded in the examined granitoids are more likely intrinsic to their parental magma sources. The enrichment in LILEs and the depletions in Nb, Ta, and Ti (Figure 7b) have plausibly resulted from enriched mantle (EM) components derived from dehydration of subducted sedimentary rocks [81].

Furthermore, the compositions of the investigated NEBs plot between the compositional fields of flood basalts and mafic rocks from active continental margins in the Th/Yb versus Ta/Yb diagram (Figure 9b). However, the NEBs show analogous geochemical signatures (i.e., Th/Ce ratio) to those of arc-related adakites (Figure 11a), suggesting that their source was different from that of crust-derived adakites. In addition, the studied NEB samples plot in the field of the Mindanao NEBs in the $Nb/La_{PM}$ versus $La/Yb_{PM}$ diagram (Figure 11b). From this diagram it also becomes evident that the compositions of the investigated NEBs bear no resemblance to those of typical OIB-like rocks from the Marquesas Island of the Philippines [82]. This implies that the investigated NEBs were most likely formed by slab-derived adakitic melts. We suggest that the examined NEBs were most likely derived from melting of mantle wedge peridotites that were variably metasomatized by slab-related adakitic melts. Similar conclusions have been reported for the adakite-NEB suites from the Central American arc [68,82].

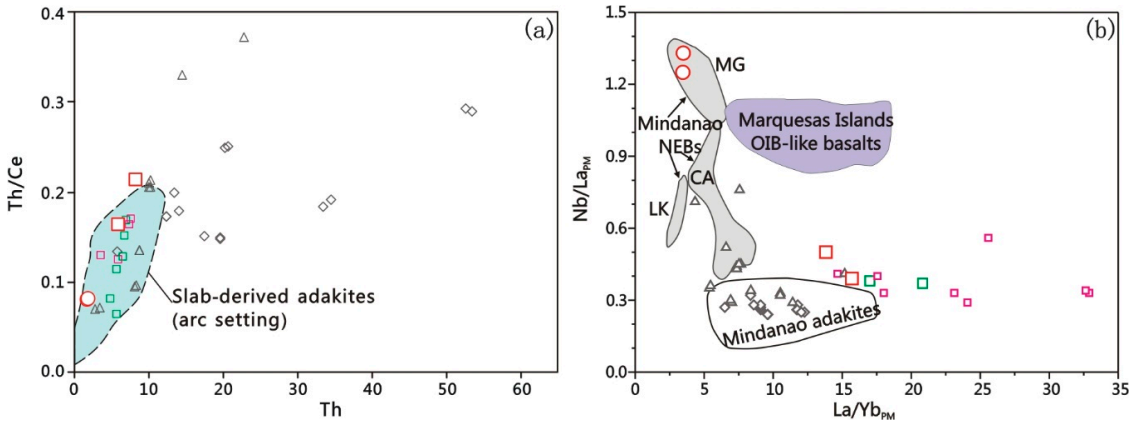



**Figure 11.** (**a**) Th/Ce versus Th diagram and (**b**) $(Nb/La)_{PM}$ versus $(La/Yb)_{PM}$ diagram. The fields for Mindanao adakites, NEBs, and Marquesas Islands OIB-like basalts are from [82]. The data sources and symbols are as in Figure 6.

Overall, our data indicate that a continental arc setting related to slab subduction is the ideal geotectonic regime for the generation of the Mesozoic granitoid rocks and NEBs from the SCS.

### *5.3. Petrogenesis*

#### 5.3.1. Granodiorites

The granodiorites of this study have evident depletions in HFSEs, in particular, significantly lower Zr + Nb + Ce + Y abundances (average 192 μg/g) than the lowest value for A-type granites (350 μg/g) [83]. In addition, the markedly depleted Sr-Nd isotope compositions of granodiorites indicate that mantle material was added to the parental magma of these rocks, which suggests that granodiorites are similar to I-type granite but quite different from S-type granite. In particular, the granodiorites are high-K calc-alkaline rocks (Figure 6b) and are characterized by low Y (<18 μg/g) and Yb (<1.9 μg/g) concentrations and high La/Yb (19.26–21.89) and Sr/Y (34.73–36.98) ratios. All these geochemical signatures are similar to those of adakitic rocks, as shown in Figure 8. Accordingly, the petrogenesis and origin of the granodiorites are most likely analogous to those of adakitic rocks.

Five petrogenetic models have been proposed to explain the genesis of adakitic magmas ([84] and references therein), including: (1) partial melting of a downgoing oceanic lithospheric slab; (2) combined crustal assimilation and fractional crystallization (AFC) of parental basaltic magmas; (3) partial melting of mafic rocks in the lower parts of a thickened crust; (4) partial melting of a stagnant slab in the mantle; and (5) partial melting of delaminated/eroded lower continental crust (LCC).

We suggest that the adakitic granodiorites from the SCS were generated by partial melting of subducted oceanic crust, based on the following evidence: (1) these granodiorites were formed in a continental arc setting, as discussed above, and (2) they show high MgO contents (1.70–1.77 wt %) and Mg# values (46.83–47.18). Partial melting of subducted basalts (metamorphosed to eclogite or amphibolite) will give adakitic melts characterized by a strong depletion in Y (relative to Sr) and Yb and high Sr/Y and La/Yb if garnet and/or amphibole are left as residue phases in the mantle source [31]. The slightly concave trend of the middle REEs in Figure 7a implies that amphibole was probably a residual phase in the mantle source region [85], which is further corroborated by the lower Nb/Ta (9.98–13.0) and higher Zr/Sm (45.32–47.69) ratios of the adakitic granodiorites compared to those of the PM (17.39 and 25.23 for Nb/Ta and Zr/Sm, respectively [86]). Moreover, fractionation of amphibole and/or garnet depletes the melt in Y relative to Sr, giving high Sr/Y, whereas fractionation of plagioclase depletes the melt in Sr relative to Y, giving low Sr/Y [31]. However, the marked depletions in HREE and Y contents of the investigated adakitic granodiorites suggest that partial melting occurred most likely in the garnet stability field, with little or no plagioclase as a residual mineral phase in the relatively deep-seated mantle source of their parental magmas [30].

Furthermore, the following lines of evidence argue against the other four conceptual petrologic models for the generation of the granodiorites:

(1) The granodiorites of this study have relatively high $\varepsilon_{Nd}(t)$ values, generally positive zircon $\varepsilon_{Hf}(t)$ values, and depleted Sr isotope compositions, all arguing against crustal assimilation. Hence, the model of crustal AFC processes of mafic magmas must be ruled out.

(2) Adakitic rocks derived from partial melting of delaminated LCC generally resemble adakites generated by slab melting in many aspects, such as their high Mg# values and La/Yb ratios [87]. However, the investigated adakitic granodiorites show generally positive zircon $\varepsilon_{Hf}(t)$ values and relatively depleted Sr isotope compositions, all indicating a significant contribution of mantle components. Furthermore, the high $Al_2O_3$ contents of the adakitic granodiorites from the SCS are inconsistent with the idea that these rocks were derived by the partial melting of LCC, which produces rocks characterized by low $Al_2O_3$ contents [88,89]. Therefore, it seems that any petrogenetic scenario emphasizing the involvement of LCC, irrespective of whether it is delaminated or thickened, cannot sufficiently explain the formation of the adakitic granodiorites from the SCS.

(3) The granodiorites yielded Mesoproterozoic Nd isotope and zircon Hf isotope model ages, suggesting that they could have formed by partial melting of a remnant Mesoproterozoic subducted lithospheric slab that stalled in the mantle. Such an origin can explain the high MgO contents, generally positive zircon $\varepsilon_{Hf}(t)$ values, and depleted Sr isotope compositions of the investigated rocks. However,

it is questionable whether such a Mesoproterozoic subducted slab could have remained in the mantle until the Late Mesozoic without being entirely consumed. Moreover, the lithosphere itself moved significantly after the Mesoproterozoic. Therefore, it seems unlikely that the stalled subducted slab would have remained in the same position relative to the convecting mantle until the Jurassic [90], especially given the superplume activity at 860–750 Ma [91] after the collision between the Yangtze and Cathaysia blocks during the Neoproterozoic (1000–900 Ma).

We note that the adakitic granodiorites of the present study have slightly higher $K_2O$ contents (3.31–3.39 wt %) and initial $^{87}Sr/^{86}Sr$ ratios (0.70541–0.70551), as well as lower Mg# and $\varepsilon_{Nd}(t)$ values (−3.62 to −3.52), than most typical adakites derived from melting of pure basaltic oceanic crust (Figure 10a) [30,90]. These features indicate input of some other components except for oceanic crustal materials to the source region of the investigated adakitic granodiorites. It is well documented that subduction zone magmatism is mainly controlled by contributions from the subducted mafic oceanic crust, the overlying subducted sediments, and the mantle wedge [92]. Aside from the subducted basaltic oceanic crust, the sedimentary lid of a subducted oceanic slab may have been another potential source contributing to the genesis of the adakitic granodiorites of the SCS. When the subducted oceanic crust began to melt, the overlying sediments also underwent melting [92]. The higher Th/La ratios (0.33–0.40) of the adakitic granodiorites compared with those of typical oceanic basalts (including MORB and OIB, <0.2) imply that their source was compositionally influenced by subducted sedimentary rocks [93]. In addition, the wide variation and multipeak distribution of the $\varepsilon_{Hf}(t)$ values of zircons separated from the investigated adakitic granodiorites (Figure 4b) indicate that their parental melts were formed by a mixture of magmas derived from basaltic oceanic crust and melts derived from inputs of subducted sedimentary materials [94]. Therefore, the source region of the studied adakitic granodiorites except for subducted basaltic oceanic crust most likely contained inputs of subducted sediments as well.

#### 5.3.2. Nb-Enriched Basalts

Basalts associated with the investigated granodiorites have high $Na_2O$, $P_2O_5$, and $TiO_2$ contents, in addition to their high Nb contents (16.2–16.7 μg/g), which are considerably higher than those of typical intra-oceanic arc basalts (Nb < 2 μg/g) [30]. Moreover, the investigated basalt samples are enriched in LREEs and HFSEs and are characterized by slight negative Nb anomalies and a marked positive Ti anomaly (Figure 7). These geochemical characteristics permit the classification of the studied basalts as NEBs, similar to those described by previous authors [31,72].

Four genetic models have been suggested to explain the petrogenesis of NEBs [95]: (1) crustal contamination by sediment incorporation in the mantle source or assimilation of continental material by ascending magmas; (2) partial melting of subducted oceanic crust; (3) partial melting of enriched mantle carrying OIB-type components; and (4) partial melting of a metasomatized by adakitic magmas mantle wedge above a subducted slab. However, the first two models have been rejected owing to obvious inconsistencies with geological and experimental data [96,97]. In general, crustal contamination would produce highly enriched LILE contents and high LILE/HFSE ratios, which is inconsistent with the high HFSE contents and low LILE/HFSE ratios of NEBs [95]. In addition, partial melting of subducted oceanic crust would produce siliceous melts with an adakitic affinity [98]. The investigated NEBs show weak negative to negligible Nb anomalies in PM-normalized multi-element patterns (Figure 7b), unlike the positive Nb and Ta anomalies that characterize typical OIBs [99]. Moreover, the lower Nb/U ratios (31.42–32.98) of the NEBs compared to those of OIB (47 ± 10) [100] rule out a possible derivation of the investigated basalts from melting of an OIB-type/plume-modified mantle source region. For those reasons, we conclude that the NEBs from the SCS were generated from partial melting of a mantle wedge that had been metasomatized by adakitic magmas derived from a subducted lithospheric slab [95,101].

We note that NEBs (or HNBs) at a global scale are closely associated with adakites, whereas adakites can occur alone [95]. This implies that the generation of NEBs is closely related to that of adakites [66]. Adakitic magma derived from melting of subducted oceanic lithospheric slab can be

produced at temperatures higher than 700 °C and depths of 75–85 km [82]. These adakitic magmas carry greater amounts of LREEs and HFSEs than hydrous fluids do and percolate through variably depleted peridotites of the overlying mantle wedge, thereby resulting in their extensive metasomatism. The hybridization between slab-derived melts and mantle wedge peridotites breaks down olivine, clinopyroxene, and spinel and precipitates Nb- and Ti-bearing pargasitic amphibole, garnet, phlogopite, Na-bearing clinopyroxene, and Fe-rich orthopyroxene [101]. Finally, heat from the convecting mantle causes partial melting of the metasomatized mantle wedge, resulting in decomposition of metasomatic minerals enriched in HFSEs (Nb, Ta, and Ti) and eventually in the generation of NEBs.

### *5.4. Geodynamic Implications*

During the Mesozoic, SE Asia was located in a transitional region between the Tethyan and circum-Pacific tectonic regimes [102]. Consequently, the question arises as whether the geodynamic status of the continental margin of SE Asia was dominated by subduction of Tethyan or paleo-Pacific oceanic lithosphere [18,102]. For instance, a model of flat-slab subduction of the paleo-Pacific oceanic lithosphere has been proposed to explain the petrogenesis of the Mesozoic igneous rocks in South China [103]. However, it is unlikely that subduction of the paleo-Pacific oceanic lithosphere and associated rollback occurred over such long time periods as 180–155 Ma [103], 165–150 Ma [16], 160–110 Ma [15], or 110–85 Ma [104], even though the possibility of repeated slab advance and retreat of the paleo-Pacific plate underneath SE China [105] cannot be entirely ruled out. Alternatively, some researchers have argued that the geotectonic evolution of the South China Block during the Late Jurassic and Early Cretaceous was controlled jointly by the northwestward subduction of the paleo-Pacific plate and the northward subduction of the Neo-Tethys plate [18]. In addition, the Cretaceous basaltic rocks of the Wuyishan Range in South China have distinct geochemical and isotope characteristics from the rest of the basalts of SE Asia. This implies that metasomatism caused by fluids/melts derived from subduction of the paleo-Pacific plate beneath the Eurasian continent might not have affected entire South China but was confined mainly to the east of the Wuyishan Range. Yet other researchers have argued that the extensional tectonic regime of South China during the Cretaceous was dominated by the northward subduction of the Neo-Tethys lithospheric plate [17,106].

Geophysical data revealed the early existence of a buried Mesozoic subduction zone along the Northern SCS continental margin [22,78]. In addition, a Mesozoic volcanic arc in the SCS continental margin has been inferred from reprocessed magnetic data and other geological information [75]. In the present study, we combine geochronological and geochemical data from a granodiorite-NEB association with the results of 38 published petrological studies on the SCS to examine which oceanic lithosphere was subducting (and how) beneath the SE Asian continental margin. The Mesozoic granitoid rocks collected from the SCS display age peaks at 155–150 Ma and 125–120 Ma (Figure 12a), indicating that two magmatic events took place in the SCS margin during the Late Mesozoic (Yanshanian period) without significant magmatic activity during the early Mesozoic (Indosinian period). This differs from the ages recorded on rocks from the contiguous onshore South China continent, which show one pronounced (160–150 Ma) and two minor Late Mesozoic age peaks (140–125 Ma and 120–105 Ma) and a minor early Mesozoic peak (240–230 Ma) (Figure 12b). These contrasting age distributions imply that the main geotectonic mechanism controlling the geodynamic status of the SE Asian continental margin during the Mesozoic differed from that controlling the South China continent. It is generally accepted that the geotectonic setting of the South China Block during the Mesozoic was related to subduction of the paleo-Pacific plate (e.g., [103]). Therefore, the geodynamic processes of the SE Asian continental margin during the Mesozoic may have involved subduction of the Neo-Tethys plate [102]. However, the region where the modern SCS is situated was formerly occupied by the Mesozoic PSCS [107]. Accordingly, the northward subduction beneath the SE Asian continental margin during the Mesozoic might have involved PSCS lithosphere as well [32].

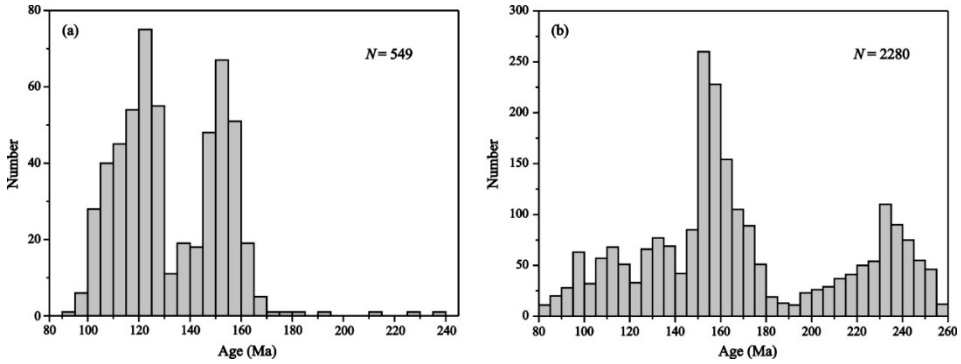



**Figure 12.** Histograms of zircon U-Pb ages of granitoid rocks from (**a**) the SCS and from (**b**) the contiguous onshore South China continent. Data for the SCS are from the present study and a compilation of previous investigations.

The granitoid rocks collected from the SCS can be classified as adakites (Figure 8). These rocks were generated during the Late Jurassic and Early Cretaceous (Supplementary Table S4). The northward subduction of the PSCS lithosphere triggered two phases of magmatic activity: the first produced the Late Jurassic adakites and some arc-like igneous rocks, and the second produced the Early Cretaceous adakites, NEBs, and arc-type magmatic rocks. The NEBs, adakites, and arc-type magmatic rocks from the SCS have Sr-Nd-Pb isotope compositions that are distinct from those of the East Pacific Rise (EPR) and the SCS MORBs (Figure 10) [64]. The Sr-Nd isotope compositions of adakites from the SCS differ not only from those of the Cenozoic adakites around the Pacific [67,68], but also from those of the Cretaceous adakites in the Lower Yangtze River Belt that were formed by partial melting of young and hot oceanic slabs subducted close to the ridge between the Pacific plate to the south and the Izanagi plate to the north (Figure 10a) [65]. More importantly, the Sr-Nd isotope compositions of adakites from the SCS are more depleted than those of the Late Mesozoic granites from the South China continent (Figure 10a) which were related to the subduction of the paleo-Pacific plate [16,91]. In addition, the Pb isotope compositions of the NEBs, adakites, and arc magmatic rocks from the SCS resemble those of Indian Ridge (IR) MORB-like rocks with a typical Dupal isotopic anomaly (Figure 10b). Furthermore, their Sr-Nd isotope compositions plot in the region between IR MORBs and Indian Ocean sediments in a $\varepsilon_{Nd}(t)$ versus $(^{87}Sr/^{86}Sr)_i$ diagram (Figure 10a). These geochemical signatures indicate that the studied rocks were compositionally analogous to those from the Mesozoic Indian Ocean (or Neo-Tethyan) crust. Considering that the Mesozoic northward subduction along the SE Asian continental margin probably involved PSCS lithosphere [32], we suggest that the Tethyan ophiolites from SE Asia [102,108], the island-arc magmatic rocks from the Meratus Range [109], and the Schwaner Range [94] in the Sundaland region, together with the PSCS, may have constituted an integrated trench–arc–basin system during the Mesozoic Era.

By the reasoning in the foregoing discussion it is inferred that the PSCS was a basin of the Neo-Tethyan Ocean during the Middle Jurassic. As a result of continuous northward subduction and drifting of the Neo-Tethys, the young (<25 Myr) and hot oceanic lithosphere of the PSCS began subducting toward the SE Asian continental margin during the Late Jurassic (Figure 13). The descending lithospheric slab underwent a phase of dehydration at shallow depths that caused fluid-fluxed partial melting of the overlying mantle wedge, producing early arc-type magmatic rocks ($J_3$). Subsequently, the subducted slab underwent partial melting at greater depths, generating adakitic magmas. These slab melts rose through the overlying mantle, carrying greater amounts of LREEs and HFSEs than the hydrous fluids. These adakitic melts interacted with the mantle wedge peridotites en route to the surface, resulting in hybridization and metasomatism of peridotites. This process led to decomposition of various mantle minerals (i.e., olivine, pyroxenes, and spinel) forming Nb-enriched minerals. Portions of the adakitic magma ascended continuously without interacting with the ambient mantle and formed the early adakites ($J_3$) (Figure 13). During the Early Cretaceous, the mid-ocean ridge (MOR) of the

PSCS was subducted further, leading to partial melting of the downgoing MOR-type crust and the formation of the late adakites ($K_1$) (Figure 13). Moreover, heat derived from the MOR not only induced partial melting of the early metasomatized mantle to form the NEBs ($K_1$) but also resulted in a second dehydration phase of the subducted slab far from the MOR. The fluid from this second dehydration stage triggered the second partial melting episode of the overlying mantle wedge and generated the late arc-derived magmatic rocks ($K_1$) (Figure 13). Finally, these rocks were dispersed to different locations as a result of the opening and spreading of the SCS during the Cenozoic Era.

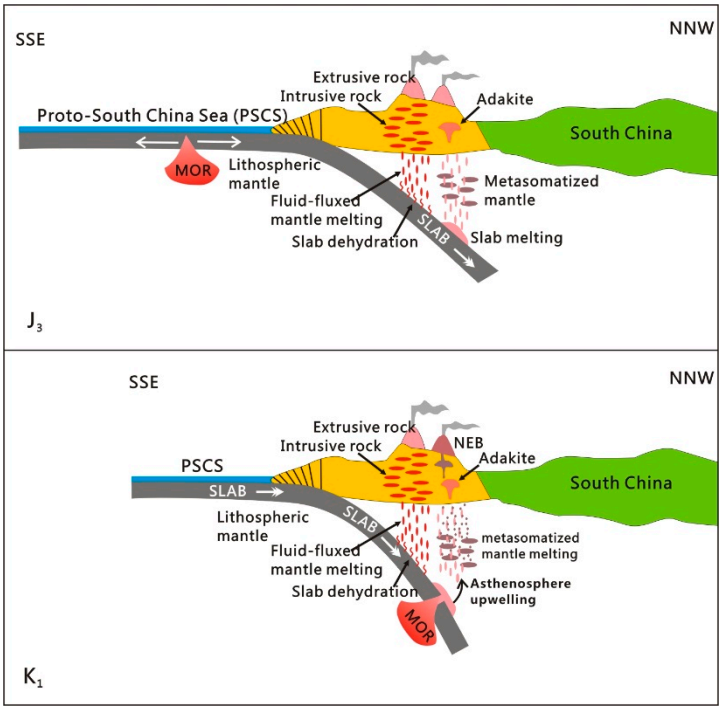



**Figure 13.** Schematic tectonic model of SE Asia during the Late Mesozoic illustrating the generation of the NEBs, adakites, and arc magmatic rocks in the SCS. During the Late Jurassic ($J_3$), the young, and thus hot, subducted oceanic lithosphere of the PSCS was dehydrated at a relatively shallow depth, which triggered fluid-fluxed partial melting of the overlying mantle wedge, producing the early arc magmatic rocks. With further subduction, the PSCS slab underwent partial melting at depth and generated the early adakites and metasomatized mantle with Nb-enriched minerals. During the Early Cretaceous ($K_1$), the mid-oceanic ridge (MOR) was subducted, and subsequently, the subducted slab broke off, leading to asthenospheric upwelling. Heat derived from the upwelling not only induced partial melting of the broken slab at its edge and of the early metasomatized mantle to form the late adakites and NEBs, respectively, but also resulted in a second dehydration event of the broken slab, far from the edge. The fluids from this second dehydration phase triggered a subsequent partial melting of the overlying mantle wedge and generated the late arc-related magmatic rocks.

## 6. Conclusions

In the present study, we determined the geochemical and geochronological signatures of adakitic granodiorites and Nb-enriched basalts (NEBs) from the Xiaozhenzhu Seamount near the Zhongnan Fault in the South China Sea (SCS). We combined our data with those from previously published works on the petrology of igneous rocks from the SCS, to infer conclusions about lithospheric subduction and related processes below the SE Asian continental margin during the Mesozoic. The investigated rocks from the SCS were formed during the Late Mesozoic, whereas those in contiguous onshore South China were generated during both the early and Late Mesozoic. The SCS magmatic rocks include not only Late Jurassic arc-related magmatic rocks and adakites, but also Early Cretaceous arc-type magmatic rocks, adakites, and NEBs, indicating that they were derived from slab subduction. We propose that the

Mesozoic magmatic rocks from the SCS are related to subduction of an early Neo-Tethyan lithospheric domain, given that (1) the SE Asian continental margin was located in a transitional area between the Neo-Tethyan and paleo-Pacific Oceans during the Mesozoic, (2) the PSCS formerly occupied the area where the modern SCS is situated, and (3) the Mesozoic magmatic rocks in South China are related to subduction of the paleo-Pacific plate. We suggest that the PSCS may be a basin of the Neo-Tethys. Compaction resulting from the northward subduction and drifting of the Neo-Tethys led the young PSCS lithosphere to subduct beneath the SE Asian continental margin during the Late Jurassic, which produced the corresponding arc-type igneous rocks and adakites in the first phase of magmatic activity. During the Early Cretaceous, ridge subduction of the PSCS triggered a second phase of magmatic activity, generating contemporaneous normal arc-related magmatic rocks, adakites, and NEBs.

**Supplementary Materials:** The following are available online at http://www.mdpi.com/2075-163X/9/10/598/s1, Table S1. In situ zircon U-Pb dating results for the granodiorite from the South China Sea; Table S2. In situ zircon Hf isotope results for the granodiorite from the South China Sea; Table S3. $^{40}Ar/^{39}Ar$ dating results for the Nb-enriched basalt from the South China Sea; Table S4. Major (wt %) and trace (μg/g) element compositions of the granitoids and NEBs from the South China Sea; Table S5. Sr-Nd-Pb isotope compositions of granitoids and NEBs from the South China Sea.

**Author Contributions:** Conceptualization, G.C., Z.W. and L.Z.; Formal Analysis, G.C. and L.Z.; Investigation, G.C., Z.W., Y.Y. and L.Z.; Data Curation, G.C. and C.Z.; Writing—Original Draft Preparation, G.C., Z.W. and L.Z.; Writing—Review and Editing, G.C., Z.W., H.Z., L.Z., and A.K.; Visualization, H.Z. and C.Z.; Funding Acquisition, G.C., Y.Y. and Z.W.

**Funding:** This work was financially supported by the Project of China Geological Survey (Grant No. DD20190627), the National Natural Science Foundation of China (Grant Nos.41576068 and 91428205), and research grants from the State Key Laboratory of Isotope Geochemistry, Guangzhou Institute of Geochemistry, Chinese Academy of Sciences (Grant No. SKLIG-KF-14-08) and the Natural Science Foundation of Guangdong Province (2018A030313168), and the Fundamental Research Funds for the Central Universities of China (Grant No. 19gpy99).

**Acknowledgments:** We thank Zhen Sun for helpful suggestions and Xianglin Tu for assistance with zircon U-Pb dating. The valuable comments and suggestions of two anonymous reviewers also helped us greatly improve our paper. Our thanks also go to the crew of the R/V Ocean No. 4 cruise carried out by the Guangzhou Marine Geological Survey (GMGS), Ministry of Natural Resources of the People's Republic of China.

**Conflicts of Interest:** The authors declare no conflict of interest.

## References

1. Hall, R. Cenozoic plate tectonic reconstructions of SE Asia. In *Petroleum Geology of Southeast Asia*; Fraser, A.J., Matthews, S.J., Murphy, R.W., Eds.; Geological Society: London, UK, 1997; pp. 11–23.
2. Zahirovic, S.; Seton, M.; Müller, R. The Cretaceous and Cenozoic tectonic evolution of Southeast Asia. *Solid Earth* **2014**, *5*, 227–273. [CrossRef]
3. Liu, W.-N.; Li, C.-F.; Li, J.; Fairhead, D.; Zhou, Z. Deep structures of the Palawan and Sulu Sea and their implications for opening of the South China Sea. *Mar. Petrol. Geol.* **2014**, *58*, 721–735. [CrossRef]
4. Chen, L.; Hu, J.W.; Yang, D.H.; Song, H.B.; Wang, Z.H. Kinematic models for the opening of the South China Sea: An upwelling divergent flow origin. *J. Geodyn.* **2017**, *107*, 20–33. [CrossRef]
5. Clift, P.; Lee, G.H.; Anh Duc, N.; Barckhausen, U.; Van Long, H.; Zhen, S. Seismic reflection evidence for a Dangerous Grounds miniplate: No extrusion origin for the South China Sea. *Tectonics* **2008**, *27*. [CrossRef]
6. Hall, R.; Breitfeld, T.H. Nature and demise of the Proto-South China Sea. *Bull. Geol. Soc. Malays.* **2017**, *63*, 61–76. [CrossRef]
7. Cullen, A.; Reemst, P.; Henstra, G.; Gozzard, S.; Ray, A. Rifting of the South China Sea: New perspectives. *Petrol. Geosci.* **2010**, *16*, 273–282. [CrossRef]
8. Rangin, C.; Bellon, H.; Benard, F.; Letouzey, J.; Muller, C.; Sanudin, T. Neogene arc continent collision in Sabah, northern Borneo (Malaysia). *Tectonophysics* **1990**, *183*, 305–319. [CrossRef]
9. Hutchison, C.S. Marginal basin evolution: The southern South China Sea. *Mar. Pet. Geol.* **2004**, *21*, 1129–1148. [CrossRef]
10. Holloway, N. The north Palawan block, Philippines: Its relation to the Asian mainland and its role in the evolution of the South China Sea. *Geol. Soc. Malays. Bull.* **1981**, *14*, 19–58. [CrossRef]

11. Hutchison, C.S. The 'Rajang accretionary prism' and 'Lupar Line' problem of Borneo. In *Tectonic Evolution of Southeast Asia*; Hall, R., Blundell, D., Eds.; Geological Society: London, UK, 1996; pp. 247–261.
12. Hall, R.; van Hattum, M.W.A.; Spakman, W. Impact of India–Asia collision on SE Asia: The record in Borneo. *Tectonophysics.* **2008**, *451*, 366–389. [CrossRef]
13. Zhou, X.M.; Li, W.X. Origin of Late Mesozoic igneous rocks in Southeastern China: Implications for lithosphere subduction and underplating of mafic magmas. *Tectonophysics* **2000**, *326*, 269–287. [CrossRef]
14. Zhao, L.; Guo, F.; Fan, W.; Zhang, Q.; Wu, Y.; Li, J.; Yan, W. Early Cretaceous potassic volcanic rocks in the Jiangnan Orogenic Belt, East China: Crustal melting in response to subduction of the Pacific–Izanagi ridge? *Chem. Geol.* **2016**, *437*, 30–43. [CrossRef]
15. Meng, L.; Li, Z.-X.; Chen, H.; Li, X.-H.; Wang, X.-C. Geochronological and geochemical results from Mesozoic basalts in southern South China Block support the flat-slab subduction model. *Lithos* **2012**, *132*, 127–140. [CrossRef]
16. Zhao, K.-D.; Jiang, S.-Y.; Yang, S.-Y.; Dai, B.-Z.; Lu, J.-J. Mineral chemistry, trace elements and Sr-Nd-Hf isotope geochemistry and petrogenesis of Cailing and Furong granites and mafic enclaves from the Qitianling batholith in the Shi-Hang zone, South China. *Gondwana Res.* **2012**, *22*, 310–324. [CrossRef]
17. Chen, W.; Chen, P.; Xu, X.; Zhang, M. Geochemical characteristics of Cretaceous basaltic rocks in South China and constraints on Pacific plate subduction. *Sci. China Ser. D Earth Sci.* **2005**, *48*, 2104–2117. [CrossRef]
18. Wang, Y.; Fan, W.; Zhang, G.; Zhang, Y. Phanerozoic tectonics of the South China Block: Key observations and controversies. *Gondwana Res.* **2013**, *23*, 1273–1305. [CrossRef]
19. Sun, Q.; Xie, X.; Piper, D.J.W.; Wu, J.; Wu, S. Three dimensional seismic anatomy of multi-stage mass transport deposits in the Pearl River Mouth Basin, northern South China Sea: Their ages and kinematics. *Mar. Geol.* **2017**, *393*, 93–108. [CrossRef]
20. Yu, Z.; Li, J.; Ding, W.; Zhang, J.; Ruan, A.; Niu, X. Crustal structure of the Southwest Subbasin, South China Sea, from wide-angle seismic tomography and seismic reflection imaging. *Mar. Geophys. Res.* **2017**, *38*, 85–104. [CrossRef]
21. Tang, Q.; Zheng, C. Crust and upper mantle structure and its tectonic implications in the South China Sea and adjacent regions. *J. Asian Earth Sci.* **2013**, *62*, 510–525. [CrossRef]
22. Sun, G.; Huang, Y.; Huang, W. Discussion location of Mesozoic paleo-subduction zone in north margin of South China Sea. *J. Cent. South Univ.* **2015**, *46*, 908–916.
23. Yan, Q.; Shi, X.; Liu, J.; Wang, K.; Bu, W. Petrology and geochemistry of Mesozoic granitic rocks from the Nansha micro-block, the South China Sea: Constraints on the basement nature. *J. Asian Earth Sci.* **2010**, *37*, 130–139. [CrossRef]
24. Xu, C.; Shi, H.; Barnes, C.G.; Zhou, Z. Tracing a late Mesozoic magmatic arc along the Southeast Asian margin from the granitoids drilled from the northern South China Sea. *Int. Geol. Rev.* **2016**, *58*, 71–94. [CrossRef]
25. Qiu, Y.; Chen, G.-N.; Liu, F.-L.; Peng, Z.-L. Discovery of granite and its tectonic significance in southwestern basin of the South China Sea. *Geol. Bull. China* **2008**, *27*, 2104–2107, (In Chinese with English abstract).
26. Zhang, Z.; Du, Y.; Gao, L.; Fang, N.; Yang, S.; Liu, J.; Song, C. The late mesozoic granodiorites from the southwest basin in the South China Sea and its tectonic implication. *J. Earth Sci.* **2012**, *23*, 268–276. [CrossRef]
27. Martin, H.; Smithies, R.; Rapp, R.; Moyen, J.-F.; Champion, D. An overview of adakite, tonalite–trondhjemite–granodiorite (TTG), and sanukitoid: Relationships and some implications for crustal evolution. *Lithos* **2005**, *79*, 1–24. [CrossRef]
28. Ma, Q.; Zheng, J.; Griffin, W.L.; Zhang, M.; Tang, H.; Su, Y.; Ping, X. Triassic "adakitic" rocks in an extensional setting (North China): Melts from the cratonic lower crust. *Lithos* **2012**, *149*, 159–173. [CrossRef]
29. Kay, R.W. Aleutian magnesian andesites: Melts from subducted Pacific ocean crust. *J. Volcanol. Geoth. Res.* **1978**, *4*, 117–132. [CrossRef]
30. Martin, H. Adakitic magmas: Modern analogues of Archaean granitoids. *Lithos* **1999**, *46*, 411–429. [CrossRef]
31. Castillo, P.R. Origin of the adakite–high-Nb basalt association and its implications for postsubduction magmatism in Baja California, Mexico. *Geol. Soc. Am. Bull.* **2008**, *120*, 451–462. [CrossRef]
32. Taylor, B.; Hayes, D.E. The Tectonic and Geologic Evolution of Southeast Asian Seas and Islands: Part 2. In *Origin and History of the South China Sea Basin*; American Geophysical Union: Washington, DC, USA, 1983; pp. 23–56.

33. Briais, A.; Patriat, P.; Tapponnier, P. Updated interpretation of magnetic anomalies and seafloor spreading stages in the south China Sea: Implications for the Tertiary tectonics of Southeast Asia. *J. Geophys. Res. Solid Earth* **1993**, *98*, 6299–6328. [CrossRef]
34. Zhou, D.; Sun, Z.; Chen, H.-Z.; Xu, H.-H.; Wang, W.-Y.; Pang, X.; Cai, D.-S.; Hu, D.-K. Mesozoic paleogeography and tectonic evolution of South China Sea and adjacent areas in the context of Tethyan and Paleo-Pacific interconnections. *Isl. Arc* **2008**, *17*, 186–207. [CrossRef]
35. Taylor, B.; Hayes, D.E. The Tectonic and Geologic Evolution of Southeast Asian Seas and Islands. In *The Tectonic Evolution of the South China Basin*; American Geophysical Union: Washington, DC, USA, 1980; pp. 89–104.
36. Gatinsky, Y.G.; Hutchison, C.S. Cathaysia, Gondwanaland, and the Paleotethys in the evolution of continental Southeast Asia. *Geol. Soc. Malays.* **1986**, *20*, 179–199. [CrossRef]
37. Cullen, A.B. Transverse segmentation of the Baram-Balabac Basin, NW Borneo: Refining the model of Borneo's tectonic evolution. *Petrol. Geosci.* **2010**, *16*, 3–29. [CrossRef]
38. Zahirovic, S.; Matthews, K.J.; Flament, N.; Müller, R.D.; Hill, K.C.; Seton, M.; Gurnis, M. Tectonic evolution and deep mantle structure of the eastern Tethys since the latest Jurassic. *Earth Sci. Rev.* **2016**, *162*, 293–337. [CrossRef]
39. Gong, Z.; Jin, Q.; Qiu, Z.; Wang, S.; Meng, J. *Geology, Tectonics and Evolution of the Pearl River Mouth Basin. Chinese Sedimentary Basins*; Elsevier: Amsterdam, The Netherlands, 1989; pp. 181–196.
40. Schlüter, H.U.; Hinz, K.; Block, M. Tectono-stratigraphic terranes and detachment faulting of the South China Sea and Sulu Sea. *Mar. Geol.* **1996**, *130*, 39–78. [CrossRef]
41. Shao, L.; You, H.; Hao, H.; Wu, G.; Qiao, P.; Lei, Y. Petrology and depositional environments of Mesozoic strata in the northeastern South China Sea. *Geol. Rev.* **2007**, *53*, 164–170, (In Chinese with English abstract).
42. Zhou, D.; Wu, S.; Chen, H. Some remarks on the tectonic evolution of Nansha and its adjacent region in southern South China Sea. *Geotecton. Metallog.* **2005**, *29*, 339–345, (In Chinese with English abstract).
43. Kudrass, H.R.; Wiedicke, M.; Cepek, P.; Kreuzer, H.; Müller, P. Mesozoic and Cainozoic rocks dredged from the South China Sea (Reed Bank area) and Sulu Sea and their significance for plate-tectonic reconstructions. *Mar. Petrol. Geol.* **1986**, *3*, 19–30. [CrossRef]
44. Fang, N. A new model on the Mesozoic "South China Sea" (SCS): Reconstructing the Hainan marginal arc and recognizing the Tethyan SCS. *Earth Sci. Front.* **2016**, *23*, 107–119, (In Chinese with English abstract).
45. Wu, S.; Zhou, D.; Liu, H. Tectonic framework and evolutionary characteristics of Nansha Block, South China Sea. *Geotecton. Metallog.* **2004**, *28*, 23–28, (In Chinese with English abstract).
46. Liu, H.; Xie, G.; Yan, P.; Liu, Y.; Zheng, H. Tectonic implication of Mesozoic marine deposits in the Nansha Islands of the South China Sea. *Oceanol. Limnol. Sin.* **2007**, *38*, 272–278, (In Chinese with English abstract).
47. Liu, Y.; Hu, Z.; Gao, S.; Gunther, D.; Xu, J.; Gao, C.; Chen, H. In situ analysis of major and trace elements of anhydrous minerals by LA-ICP-MS without applying an internal standard. *Chem. Geol.* **2008**, *257*, 34–43. [CrossRef]
48. Liu, Y.; Gao, S.; Hu, Z.; Gao, C.; Zong, K.; Wang, D. Continental and Oceanic Crust Recycling-induced Melt-Peridotite Interactions in the Trans-North China Orogen: U-Pb Dating, Hf Isotopes and Trace Elements in Zircons from Mantle Xenoliths. *J. Petrol.* **2010**, *51*, 537–571. [CrossRef]
49. Ludwig, K.R. *User's Manual for Isoplot 3.70: A Geochronological Toolkit for Microsoft Excel*; Berkeley Geochronology Center: Berkeley, CA, USA, 2008.
50. Griffin, W.L.; Pearson, N.J.; Belousova, E.; Jackson, S.E.; van Achterbergh, E.; O'Reilly, S.Y.; Shee, S.R. The Hf isotope composition of cratonic mantle: LAM-MC-ICPMS analysis of zircon megacrysts in kimberlites. *Geochim. Cosmochim. Acta* **2000**, *64*, 133–147. [CrossRef]
51. Koppers, A.A.P. ArArCALC—Software for $^{40}Ar/^{39}Ar$ age calculations. *Comput. Geosci.* **2002**, *28*, 605–619. [CrossRef]
52. Lee, J.-Y.; Marti, K.; Severinghaus, J.P.; Kawamura, K.; Yoo, H.-S.; Lee, J.B.; Kim, J.S. A redetermination of the isotopic abundances of atmospheric Ar. *Geochim. Cosmochim. Acta* **2006**, *70*, 4507–4512. [CrossRef]
53. Steiger, R.H.; Jäger, E. Subcommission on geochronology: Convention on the use of decay constants in geo- and cosmochronology. *Earth Planet. Sci. Lett.* **1977**, *36*, 359–362. [CrossRef]
54. Li, X.; Qi, C.; Liu, Y.; Liang, X.; Tu, X.; Xie, L.; Yang, Y. Petrogenesis of the Neoproterozoic bimodal volcanic rocks along the western margin of the Yangtze Block: New constraints from Hf isotopes and Fe/Mn ratios. *Chin. Sci. Bull.* **2005**, *50*, 2481–2486. [CrossRef]

55. Sun, S.S.; McDonough, W.F. *Chemical and Isotopic Systematics of Oceanic Basalts: Implications for Mantle Composition and Processes*; Geological Society: London, UK, 1989; pp. 313–345.
56. Defant, M.J.; Drummond, M.S. Derivation of some modern arc magmas by melting of young subducted lithosphere. *Nature* **1990**, *347*, 662. [CrossRef]
57. Petford, N.; Atherton, M. Na-rich Partial Melts from Newly Underplated Basaltic Crust: The Cordillera Blanca Batholith, Peru. *J. Petrol.* **1996**, *37*, 1491–1521. [CrossRef]
58. Pearce, J.A.; Harris, N.B.W.; Tindle, A.G. Trace Element Discrimination Diagrams for the Tectonic Interpretation of Granitic Rocks. *J. Petrol.* **1984**, *25*, 956–983. [CrossRef]
59. Pearce, J.A. The role of sub-continental lithosphere in magma genesis at destructive plate margins. In *Continental Basalts and Mantle Xenoliths*; Hawkesworth, C.J., Norry, H.J., Eds.; Shiva Publications: Chandigarh, India, 1983; pp. 230–249.
60. Yan, Q.; Shi, X.; Li, N. Oxygen and lead isotope characteristics of granitic rocks from the Nansha block (South China Sea): Implications for their petrogenesis and tectonic affinity. *Isl. Arc* **2011**, *20*, 150–159. [CrossRef]
61. Yan, Q.; Shi, X.; Castillo, P.R. The late Mesozoic–Cenozoic tectonic evolution of the South China Sea: A petrologic perspective. *J. Asian Earth Sci.* **2014**, *85*, 178–201. [CrossRef]
62. Shen, W.-Z.; Ling, H.-F.; Tao, T. Sr-Nd isotope geochemistry of the Late Mesozoic granite-volcanics in South China. In *Genesis and Lithospheric Dynamics of Late Mesozoic Granites in Nanling Area: Beijing*; Zhou, X.-M., Ed.; Science Press: Beijing, China, 2007; pp. 123–160. (In Chinese)
63. Zhong, L.; Cai, G.; Koppers, A.P.A.; Xu, Y.; Xu, H.; Gao, H.; Xia, B. $^{40}Ar/^{39}Ar$ dating of oceanic plagiogranite: Constraints on the initiation of seafloor spreading in the South China Sea. *Lithos* **2018**, *302*, 421–426. [CrossRef]
64. Zhang, G.-L.; Chen, L.-H.; Jackson, M.G.; Hofmann, A.W. Evolution of carbonated melt to alkali basalt in the South China Sea. *Nat. Geosci.* **2017**, *10*, 229. [CrossRef]
65. Ling, M.-X.; Wang, F.-Y.; Ding, X.; Hu, Y.-H.; Zhou, J.-B.; Zartman, R.E.; Yang, X.-Y.; Sun, W. Cretaceous ridge subduction along the Lower Yangtze River Belt, Eastern China. *Econ. Geol.* **2009**, *104*, 303–321. [CrossRef]
66. Defant, M.J.; Jackson, T.E.; Drummond, M.S.; De Boer, J.Z.; Bellon, H.; Feigenson, M.D.; Maury, R.C.; Stewart, R.H. The geochemistry of young volcanism throughout western Panama and southeastern Costa Rica: An overview. *J. Geol. Soc.* **1992**, *149*, 569–579. [CrossRef]
67. Sajona, F.G.; Maury, R.C.; Pubellier, M.; Leterrier, J.; Bellon, H.; Cotten, J. Magmatic source enrichment by slab-derived melts in a young post-collision setting, central Mindanao (Philippines). *Lithos* **2000**, *54*, 173–206. [CrossRef]
68. Aguillón-Robles, A.; Calmus, T.; Benoit, M.; Bellon, H.; Maury, R.C.; Cotten, J.; Bourgois, J.; Michaud, F. Late Miocene adakites and Nb-enriched basalts from Vizcaino Peninsula, Mexico: Indicators of East Pacific Rise subduction below southern Baja California? *Geology* **2001**, *29*, 531–534. [CrossRef]
69. Ben Othman, D.; White, W.M.; Patchett, J. The geochemistry of marine sediments, island arc magma genesis, and crust-mantle recycling. *Earth Planet. Sci. Lett.* **1989**, *94*, 1–21. [CrossRef]
70. Gasparon, M.; Varne, R. Crustal assimilation versus subducted sediment input in west Sunda arc volcanics: An evaluation. *Miner. Petrol.* **1998**, *64*, 89–117. [CrossRef]
71. Liu, E.; Wang, X.-C.; Zhao, J.-X.; Wang, X. Geochemical and Sr–Nd isotopic variations in a deep-sea sediment core from Eastern Indian Ocean: Constraints on dust provenances, paleoclimate and volcanic eruption history in the last 300,000 years. *Mar. Geol.* **2015**, *367*, 38–49. [CrossRef]
72. Polat, A.; Kerrich, R. Magnesian andesites, Nb-enriched basalt-andesites, and adakites from late-Archean 2.7 Ga Wawa greenstone belts, Superior Province, Canada: Implications for late Archean subduction zone petrogenetic processes. *Contrib. Miner. Petr.* **2001**, *141*, 36–52. [CrossRef]
73. Defant, M.J.; Drummond, M.S. Mount St. Helens: Potential example of the partial melting of the subducted lithosphere in a volcanic arc. *Geology* **1993**, *21*, 547–550. [CrossRef]
74. Kepezhinskas, P.; Defant, M.J.; Drummond, M.S. Progressive enrichment of island arc mantle by melt-peridotite interaction inferred from Kamchatka xenoliths. *Geochim. Cosmochim. Acta* **1996**, *60*, 1217–1229. [CrossRef]
75. Li, F.; Sun, Z.; Yang, H. Possible Spatial Distribution of the Mesozoic Volcanic Arc in the Present-Day South China Sea Continental Margin and Its Tectonic Implications. *J. Geophys Res. Solid Earth* **2018**, *123*, 6215–6235. [CrossRef]

76. Jiang, Y.-H.; Jiang, S.-Y.; Dai, B.-Z.; Liao, S.-Y.; Zhao, K.-D.; Ling, H.-F. Middle to late Jurassic felsic and mafic magmatism in southern Hunan province, southeast China: Implications for a continental arc to rifting. *Lithos* **2009**, *107*, 185–204. [CrossRef]
77. Zhou, D.; Wang, W.; Wang, J.; Pang, X.; Cai, D.; Sun, Z. Mesozoic subduction-accretion zone in northeastern South China Sea inferred from geophysical interpretations. *Sci. China Ser. D Earth Sci.* **2006**, *49*, 471. [CrossRef]
78. Min, H.; Ren, J.; Gao, J.; Zuo, Y. Location of the ancient subduction zone in the Northern South China Sea and its constrains on the spreading of the South China Sea Basin. *Geotecton. Metallog.* **2010**, *34*, 599–605.
79. Zhou, X.M.; Sun, T.; Shen, W.Z.; Shu, L.S.; Niu, Y.L. Petrogenesis of Mesozoic granitoids and volcanic rocks in south China: A response to tectonic evolution. *Episodes* **2006**, *29*, 26–33. [CrossRef]
80. Klemme, S.; Prowatke, S.; Hametner, K.; Günther, D. Partitioning of trace elements between rutile and silicate melts: Implications for subduction zones. *Geochim. Cosmochim. Acta* **2005**, *69*, 2361–2371. [CrossRef]
81. Zhong, L.; Li, J.; Peng, T.; Xia, B.; Liu, L. Zircon U-Pb geochronology and Sr-Nd-Hf isotopic compositions of the Yuanzhuding granitoid porphyry within the Shi-Hang Zone, South China: Petrogenesis and implications for Cu-Mo mineralization. *Lithos* **2013**, *177*, 402–415. [CrossRef]
82. Sajona, F.G.; Maury, R.C.; Bellon, H.; Cotten, J.; Defant, M. High Field Strength Element Enrichment of Pliocene—Pleistocene Island Arc Basalts, Zamboanga Peninsula, Western Mindanao (Philippines). *J. Petrol.* **1996**, *37*, 693–726. [CrossRef]
83. Whalen, J.B.; Currie, K.L.; Chappell, B.W. A-type granites: Geochemical characteristics, discrimination and petrogenesis. *Contrib. Mineral. Petr.* **1987**, *95*, 407–419. [CrossRef]
84. Wang, Q.; Xu, J.-F.; Jian, P.; Bao, Z.-W.; Zhao, Z.-H.; Li, C.-F.; Xiong, X.-L.; Ma, J.-L. Petrogenesis of Adakitic Porphyries in an Extensional Tectonic Setting, Dexing, South China: Implications for the Genesis of Porphyry Copper Mineralization. *J. Petrol.* **2006**, *47*, 119–144. [CrossRef]
85. Gromet, P.; Silver, L.T. REE Variations Across the Peninsular Ranges Batholith: Implications for Batholithic Petrogenesis and Crustal Growth in Magmatic Arcs. *J. Petrol.* **1987**, *28*, 75–125. [CrossRef]
86. Foley, S.; Tiepolo, M.; Vannucci, R. Growth of early continental crust controlled by melting of amphibolite in subduction zones. *Nature* **2002**, *417*, 837–840. [CrossRef] [PubMed]
87. Xu, J.-F.; Shinjo, R.; Defant, M.J.; Wang, Q.; Rapp, R.P. Origin of Mesozoic adakitic intrusive rocks in the Ningzhen area of east China: Partial melting of delaminated lower continental crust? *Geology* **2002**, *30*, 1111–1114. [CrossRef]
88. Atherton, M.P.; Petford, N. Generation of sodium-rich magmas from newly underplated basaltic crust. *Nature* **1993**, *362*, 144–146. [CrossRef]
89. Drummond, M.S.; Defant, M.J.; Kepezhinskas, P.K. Petrogenesis of slab-derived trondhjemite–tonalite–dacite/adakite magmas. *Earth Environ. Sci. Trans. R. Soc. Edinb.* **1996**, *87*, 205–215.
90. Wang, Q.; Wyman, D.A.; Xu, J.; Jian, P.; Zhao, Z.; Li, C.; Xu, W.; Ma, J.; He, B. Early Cretaceous adakitic granites in the Northern Dabie Complex, central China: Implications for partial melting and delamination of thickened lower crust. *Geochim. Cosmochim. Acta* **2007**, *71*, 2609–2636. [CrossRef]
91. Li, Z.-X.; Li, X.-H.; Zhou, H.; Kinny, P.D. Grenvillian continental collision in south China: New SHRIMP U-Pb zircon results and implications for the configuration of Rodinia. *Geology* **2002**, *30*, 163–166. [CrossRef]
92. Chauvel, C.; Lewin, E.; Carpentier, M.; Arndt, N.T.; Marini, J.-C. Role of recycled oceanic basalt and sediment in generating the Hf–Nd mantle array. *Nat. Geosci.* **2008**, *1*, 64–67. [CrossRef]
93. Plank, T. Constraints from Thorium/Lanthanum on Sediment Recycling at Subduction Zones and the Evolution of the Continents. *J. Petrol.* **2005**, *46*, 921–944. [CrossRef]
94. Kemp, A.I.S.; Hawkesworth, C.J.; Foster, G.L.; Paterson, B.A.; Woodhead, J.D.; Hergt, J.M.; Gray, C.M.; Whitehouse, M.J. Magmatic and crustal differentiation history of granitic rocks from Hf-O isotopes in zircon. *Science* **2007**, *315*, 980–983. [CrossRef] [PubMed]
95. Zhang, H.; Niu, H.; Sato, H.; Yu, X.; Shan, Q.; Zhang, B.; Ito, J.I.; Nagao, T. Late Paleozoic adakites and Nb-enriched basalts from northern Xinjiang, northwest China: Evidence for the southward subduction of the Paleo-Asian Oceanic Plate. *Isl. Arc* **2005**, *14*, 55–68. [CrossRef]
96. Rapp, R.P.; Watson, E.B.; Miller, C.F. Partial melting of amphibolite/eclogite and the origin of Archean trondhjemites and tonalites. *Precambrian Res.* **1991**, *51*, 1–25. [CrossRef]

97. Shen, X.-M.; Zhang, H.-X.; Wang, Q.; Ma, L.; Yang, Y.-H. Early Silurian (~440Ma) adakitic, andesitic and Nb-enriched basaltic lavas in the southern Altay Range, Northern Xinjiang (western China): Slab melting and implications for crustal growth in the Central Asian Orogenic Belt. *Lithos* **2014**, *206*, 234–251. [CrossRef]
98. Hastie, A.R.; Mitchell, S.F.; Kerr, A.C.; Minifie, M.J.; Millar, I.L. Geochemistry of rare high-Nb basalt lavas: Are they derived from a mantle wedge metasomatised by slab melts? *Geochim. Cosmochim. Acta* **2011**, *75*, 5049–5072. [CrossRef]
99. Ji, W.-Q.; Wu, F.-Y.; Chung, S.-L.; Wang, X.-C.; Liu, C.-Z.; Li, Q.-L.; Liu, Z.-C.; Liu, X.-C.; Wang, J.-G. Eocene Neo-Tethyan slab breakoff constrained by 45 Ma oceanic island basalt–type magmatism in southern Tibet. *Geology* **2016**, *44*, 283–286. [CrossRef]
100. Hofmann, A.W.; Jochum, K.P.; Seufert, M.; White, W.M. Nb and Pb in oceanic basalts: New constraints on mantle evolution. *Earth Planet. Sci. Lett.* **1986**, *79*, 33–45. [CrossRef]
101. Rajanikanta Singh, M.; Manikyamba, C.; Ganguly, S.; Ray, J.; Santosh, M.; Dhanakumar Singh, T.; Chandan Kumar, B. Paleoproterozoic arc basalt-boninite-high magnesian andesite-Nb enriched basalt association from the Malangtoli volcanic suite, Singhbhum Craton, eastern India: Geochemical record for subduction initiation to arc maturation continuum. *J. Asian Earth Sci.* **2017**, *134*, 191–206. [CrossRef]
102. Metcalfe, I. Gondwana dispersion and Asian accretion: Tectonic and palaeogeographic evolution of eastern Tethys. *J. Asian Earth Sci.* **2013**, *66*, 1–33. [CrossRef]
103. Li, Z.-X.; Li, X.-H. Formation of the 1300-km-wide intracontinental orogen and postorogenic magmatic province in Mesozoic South China: A flat-slab subduction model. *Geology* **2007**, *35*, 179–182. [CrossRef]
104. He, Z.-Y.; Xu, X.-S. Petrogenesis of the Late Yanshanian mantle-derived intrusions in southeastern China: Response to the geodynamics of paleo-Pacific plate subduction. *Chem. Geol.* **2012**, *328*, 208–221. [CrossRef]
105. Jiang, Y.-H.; Wang, G.-C.; Liu, Z.; Ni, C.-Y.; Qing, L.; Zhang, Q. Repeated slab advance–retreat of the Palaeo-Pacific plate underneath SE China. *Int. Geol. Rev.* **2015**, *57*, 472–491. [CrossRef]
106. Sun, W. Initiation and evolution of the South China Sea: An overview. *Acta Geochim.* **2016**, *35*, 215–225. [CrossRef]
107. Hall, R. Contraction and extension in northern Borneo driven by subduction rollback. *J. Asian Earth Sci.* **2013**, *76*, 399–411. [CrossRef]
108. Pubellier, M.; Monnier, C.; Maury, R.; Tamayo, R. Plate kinematics, origin and tectonic emplacement of supra-subduction ophiolites in SE Asia. *Tectonophysics* **2004**, *392*, 9–36. [CrossRef]
109. Yuwono, Y.S.; Priyomarsono, S.; Maury, R.C.; Rampnoux, J.P.; Soeria-Atmadja, R.; Bellon, H.; Chotin, P. Petrology of the Cretaceous magmatic rocks from Meratus Range, southeast Kalimantan. *J. Southeast Asian Earth Sci.* **1988**, *2*, 15–22. [CrossRef]




© 2019 by the authors. Licensee MDPI, Basel, Switzerland. This article is an open access article distributed under the terms and conditions of the Creative Commons Attribution (CC BY) license (http://creativecommons.org/licenses/by/4.0/).